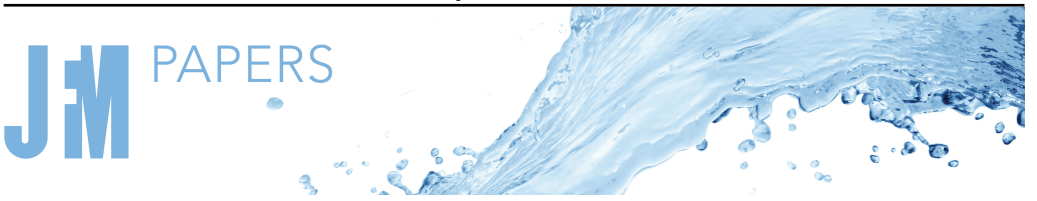
J. Fluid Mech. (2025), *vol.* 1025, A2, doi:10.1017/jfm.2025.10881



Magneto-gravity-precessional instability

Abdelaziz Salhi[1], **Waleed Mouhali**[2], **Dhaou Lassoued**[3] and **Thierry Lehner**[4]

[1]Faculté des Sciences de Tunis, Université Tunis El Manar, El Manar 2092, Tunisia

[2]ECE Paris-Ecole d'ingénieurs, 10 Rue Sextius-Michel. CS 71520, 75725 Paris CEDEX 15, France

[3]Département de Mathématique, Faculté des Sciences de Gabes, Université de Gabes, 6072 Gabes, Tunisia

[4]Laboratory for the study of the Universe and eXtreme phenomena (LUX), Observatoire de Paris, Université PSL et Paris Cité CNRS (UMR-8102), 5 place Jules Janssen, Meudon 1F-92195 Meudon CEDEX, France

Corresponding author: Abdelaziz Salhi, salhidec55@gmail.com

(Received 6 June 2025; revised 8 September 2025; accepted 10 October 2025)

Magneto-gravity-precessional instability, which results from the excitation of resonant magneto-inertia-gravity (MIG) waves by a background shear generic to precessional flows, is addressed here. Two simple background precession flows, that of Kerswell (1993 *Geophys. Astrophys. Fluid Dyn*. vol 72, no. 1–4, pp. 107–144), and that of Mahalov (1993 *Phys. Fluids A: Fluid Dyn*. vol. 5, no. 4, pp. 891–900), are considered. We analytically perform an asymptotic analysis to order $O(\varepsilon)$, where ε denotes the Poincaré number, i.e. the precession parameter, and determine the maximum growth rate of the destabilizing subharmonic resonances of MIG waves: that between two fast modes, that between two slow modes and that between a fast mode and a slow mode (mixed modes). The domains of the $(K_0B_0/\Omega_0, N/\Omega_0)$-plane for which this instability operates are identified, where $1/K_0$ denotes a characteristic length scale, B_0 is the unperturbed Alfvén velocity, Ω_0 is the rotation rate and N denotes the Brunt–Väisälä frequency. We demonstrate that the $N \to 0$ limit is, in fact, singular (discontinuous). At large K_0B_0/Ω_0, stable stratification acts to suppress the destabilizing resonance between two fast modes as well as that between two slow modes, whereas it revives the destabilizing resonance between a fast mode and a slow mode provided $N < \Omega_0$, because, without stratification, the maximal growth rate of this instability approaches zero as $K_0B_0/\Omega_0 \to +\infty$. This would be relevant for the generation of the mean electromotive force, and hence, the α-effect in helical magnetized precessional flows under weak stable stratification. Diffusive effects on the instability is considered in the simple case where the magnetic and thermal Prandtl numbers are both equal to one.

Key words: parametric instability, MHD turbulence, stratified turbulence

© The Author(s), 2025. Published by Cambridge University Press. This is an Open Access article, distributed under the terms of the Creative Commons Attribution licence (https://creativecommons.org/licenses/by/4.0/), which permits unrestricted re-use, distribution and reproduction, provided the original article is properly cited.

https://doi.org/10.1017/jfm.2025.10881 Published online by Cambridge University Press

1. Introduction

Many geophysical and astrophysical systems have magnetic fields and undergo rapid rotation; they are certainly likely to support magneto-inertia (or magneto-Coriolis (MC)) waves. The inertial waves, which are often observed in natural rotating fluid systems, arise from the intrinsic properties of a rotating fluid where the Coriolis force provides the restoring mechanism (see, e.g. Greenspan 1969). Alfvén (or hydromagnetic) waves are found in plasma (such as the solar corona) or fluids with high electrical conductivity (such as the Earth's core, (see, e.g. Finlay *et al.* 2010)). They are incompressible transverse oscillations that propagate along field lines with magnetic tension as the restoring force (see, e.g. Tomczyk *et al.* 2007). In the laboratory experiment of a magnetized turbulent Taylor–Couette flow of liquid metal by Nornberg *et al.* (2010), the combined fast and slow MC waves were clearly identified where the observed slow MC wave is damped. Magneto-inertia-gravity (MIG) waves, also called magnetic-Archimedean–Coriolis waves (see, e.g. Fearn & Proctor 1983; Buffett, Knezek & Holme 2016; Salhi *et al.* 2017, 2024; Mouhali *et al.* 2024), are disturbances that propagate in rotating and stratified magnetized flows, where the combinations of the Coriolis force, the buoyancy force and the magnetic tension provide the restoring mechanism.

In the present study, we present analytical developments characterizing some parametric instabilities occurring in stratified precessing magnetized flows: the subharmonic instabilities resulting from the excitation of resonant MIG waves by a background shear generic to precessional flows (see, e.g. Kerswell 1993; Mahalov 1993; Mason & Kerswell 2002). Indeed, the precession-driven dynamics represents a possible candidate for the development of both three-dimensional (3-D) waves with embedded two-dimensional (2-D) vortices that are present in several astrophysical and geophysical systems (see, e.g. Glampedakis, Andersson & Jones 2008; Barker 2016*a*; Khlifi *et al.* 2018; Pizzi *et al.* 2022; Kumar *et al.* 2024).

The problem of precessionally driven flow in a rotating container has been the subject of several experimental, theoretical and numerical studies for many decades considering spherical and spheroidal geometries (see, e.g. Poincaré 1910; Busse 1968; Kerswell 1993; Zhang, Chan & Liao 2014; Cébron *et al.* 2019; Lam, Kong & Zhang 2021) as well as cylindrical geometries (see, e.g. Gans 1970; Vladimirov & Tarassov 1984; Mahalov 1993; Lehner *et al.* 2010; Mouhali *et al.* 2012; Gao *et al.* 2021; Giesecke *et al.* 2024).

In a purely hydrodynamical context, flows within precessing containers result from the complex interplay between inertial waves, Ekman boundary layers and the base flow. They can eventually become unstable and create space-filling turbulence (see, e.g. Malkus 1968). Three kinds of instabilities have been suggested for precession-driven flows: boundary layer instabilities (see, e.g. Lorenzani & Tilgner 2001; Buffett 2021), bulk parametric instabilities (see, e.g. Kerswell 1993; Lin, Noir & Jackson 2014; Burmann & Noir 2022)) and centrifugal instabilities (see, e.g. Giesecke *et al.* 2019).

Directly relevant to the problem with precession and shear is the special case of Poincaré's (1910) elegant constant-vorticity solution for a precessing, oblate spheroid, addressed by Kerswell (1993). As an idealization of a small-scale disturbance evolving at the centre of a precessing spheroid, Kerswell (1993) considered an unbounded basic flow, so that the effect of boundaries are ignored, in the precessing frame, of sheared circular streamlines,

$$\boldsymbol{U} = \Omega_0\big(-y\hat{\boldsymbol{x}} + (x - 2\varepsilon z)\hat{\boldsymbol{y}}\big), \quad \boldsymbol{\Omega}_p = \Omega_p\hat{\boldsymbol{x}} = \Omega_0\varepsilon\hat{\boldsymbol{x}}, \tag{1.1}$$

where $\boldsymbol{U}$ is the velocity field of the precessing flow, $\boldsymbol{x} = x\hat{\boldsymbol{x}} + y\hat{\boldsymbol{y}} + z\hat{\boldsymbol{z}}$ denotes the vector position, $(\hat{\boldsymbol{x}}, \hat{\boldsymbol{y}}, \hat{\boldsymbol{z}})$ is an orthonormal basis of the precessing frame, Ω_0 is the solid body rotation rate (a positive constant) and $\varepsilon = \Omega_p/\Omega_0$ denotes the Poincaré parameter

https://doi.org/10.1017/jfm.2025.10881 Published online by Cambridge University Press

(a constant). In their study of nonlinear dynamics in a precessing plane fluid layer, Mason & Kerswell (2002) used the background flow (1.1) with stress-free boundary conditions.

The base flow (1.1) is an exact incompressible solution of the Navier–Stokes equation. It can be split into two parts: one part corresponding to a solid body rotation around $\hat{\boldsymbol{z}}$ with circular streamlines and the other part corresponding to a plane linear shear $\boldsymbol{U}_s = -2\Omega_0\varepsilon z\hat{\boldsymbol{y}}$. A physical interpretation of the modified flow can be found here, as also in Salhi & Cambon (2009): the misalignment of the basic 'rapid' angular velocity $\boldsymbol{W}_0 = \boldsymbol{\nabla}\times\boldsymbol{U}(\varepsilon=0)$ and the precessional one $\boldsymbol{\Omega}_p$, treated as an external Coriolis force, induces a gyroscopic torque. This torque can be exactly balanced by the plane shear $\boldsymbol{U}_s$. We note that Wiener *et al.* (1990), who studied experimentally the stability of Taylor–Couette flow subject to an external Coriolis force, have observed an axial component in the initial flow, and a transition to turbulence for larger rotation rates. Mahalov (1993) conjectured that this transition is indicative of parametric instabilities developing within the flow. Hereafter, the solution (1.1) is referred to as Kerswell's base flow (KBF).

By using the formalism with projection of the disturbance fields onto Kelvin modes, Kerswell (1993) demonstrate the local (parametric) instability of these sheared circular streamlines to the straining field present, confirming that the effect of boundaries is largely secondary. The Kelvin modes are essentially 3-D Fourier modes, even if the wavevector $\boldsymbol{k}(t)$ can become time-dependent following the mean flow streamlines. The time dependency of the wavevector represents the advection of the plane wave $\exp(\mathrm{i}\boldsymbol{k}(t)\cdot\boldsymbol{x})$ by the base flow (see, e.g. Cambon, Teissedre & Jeandel 1985; Bayly 1986; Craik & Criminale 1986). Note that the system of equations for disturbances in terms of Fourier (or Lagrangian) modes is recovered for small-scale disturbances travelling near any smooth base-flow trajectory, in the zonal asymptotic method of Lifschitz & Hameiri (1991) with close connection with geometric optics: the velocity gradients of the base flow are treated as space-uniform in a domain of unspecified length scale, asymptotically small.

The mechanism of the parametric precessional instability is similar to that which underlies the elliptical instability (Bayly 1986; Pierrehumbert 1986): a resonance in which a pair of normal modes of oscillation on the undistorted circular flow become tuned to the underlying strain field. A review of different physical aspects of the elliptical instability in the theory of turbulence and in geophysics and astrophysics was done by Kerswell (2002) (also see the recent study by McKeown *et al.* 2020), and the study of the magneto-gravity-elliptic (MGE) instability by Salhi & Cambon (2023) (hereafter SC23).

Another simple example of a generic precessing flow is that considered by Mahalov (1993): an infinite column in which a tilted (sheared) streamline solution can exist under precession (see figure 1),

$$\boldsymbol{U} = (\Omega_0 r)\hat{\boldsymbol{\varphi}} - 2(\Omega_0\varepsilon r\sin\varphi)\hat{\boldsymbol{z}}, \quad \boldsymbol{\Omega}_p = \Omega_0\varepsilon\left((\cos\varphi)\hat{\boldsymbol{r}} - (\sin\varphi)\hat{\boldsymbol{\varphi}}\right) = \Omega_0\varepsilon\hat{\boldsymbol{x}}, \tag{1.2}$$

where (r, φ, z) denotes a cylindrical coordinate system of an orthonormal basis $(\hat{\boldsymbol{r}}, \hat{\boldsymbol{\varphi}}, \hat{\boldsymbol{z}})$. An associated boundary condition is that there is no flow through the boundaries. By means of a classical normal mode analysis of small disturbances (Drazin & Reid 2004), Mahalov (1993) showed that this distortion leads to 3-D parametric instabilities. In a Cartesian coordinate system of the orthonormal basis $(\hat{\boldsymbol{x}}, \hat{\boldsymbol{y}}, \hat{\boldsymbol{z}})$, Mahalov's solution can be rewritten as (see Salhi & Cambon 2009),

$$\boldsymbol{U} = \Omega_0\left(-y\hat{\boldsymbol{x}} + x\hat{\boldsymbol{y}} - 2\varepsilon y\hat{\boldsymbol{z}}\right), \quad \boldsymbol{\Omega}_p = \Omega_p\hat{\boldsymbol{x}} = \Omega_0\varepsilon\hat{\boldsymbol{x}}, \tag{1.3}$$

ignoring the boundary conditions. The latter unbounded base flow, which is an exact solution of the incompressible Navier–Stokes equation, can similarly model localized patches of precessing columns. Hereafter it is referred to as Mahalov's base flow (MBF).

https://doi.org/10.1017/jfm.2025.10881 Published online by Cambridge University Press

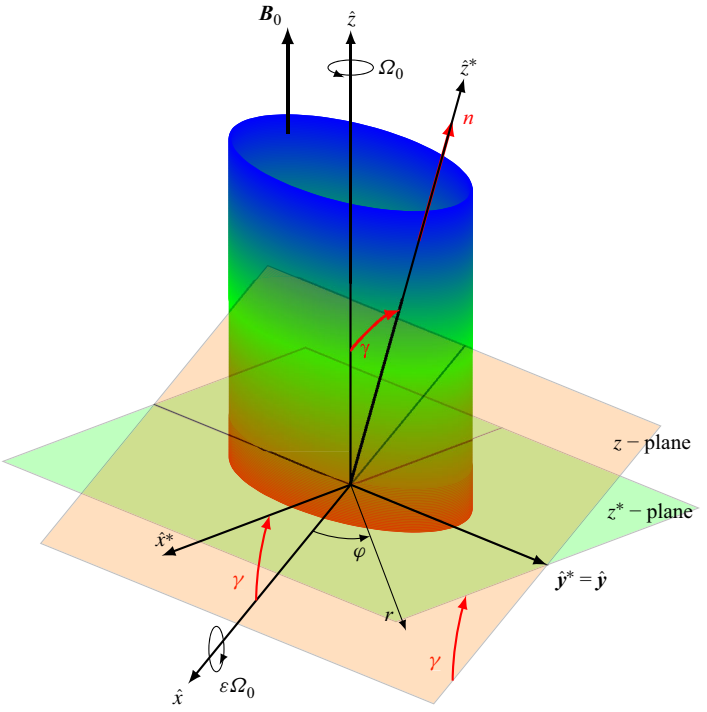


Figure 1. A slice of a vertical stratified precessing fluid column: a rotating fluid column seen in a frame rotating uniformly about the $\hat{\boldsymbol{x}}$-axis with rate $\Omega_p = \varepsilon\Omega_0$ where ε is the Poincaré number. Without precession ($\varepsilon = 0$), the unperturbed base flow, $\boldsymbol{U} = \Omega_0 r\hat{\varphi}$, has circular streamlines, and the isodensity planes are perpendicular to the vertical axis $\hat{z}$, $\boldsymbol{\nabla}\varrho(z) = -(\rho_0/g)N^2\hat{\boldsymbol{z}}$, where $N^2 = \text{const.} > 0$ is the square of the Brunt–Väisälä frequency. The effect of the Coriolis force induces a vertical mean shear that acts to balance the gyroscopic torque, so that the unperturbed velocity profile becomes $\boldsymbol{U} = \Omega_0 r(\hat{\boldsymbol{\varphi}} - 2\varepsilon \sin\varphi\hat{\boldsymbol{z}}) = \Omega_0(-y\hat{\boldsymbol{x}} + x\hat{\boldsymbol{y}} - 2\varepsilon\hat{\boldsymbol{z}})$. The trajectory of a fluid particle is in the plane perpendicular to the z^*-axis and it is an ellipse (see § 2.2.1). The plane (x^*, z^*) is obtained by a rotation, of angle $\gamma = -\tan^{-1}(2\varepsilon)$, of the plane (x, z) around the y-axis. Moreover, in the presence of the Coriolis force, the isodensity planes are perpendicular to the z^*-axis, so that $\boldsymbol{\nabla}\varrho(z^*) = -(\rho_0/g)N^2\hat{\boldsymbol{z}}^*$ with $\boldsymbol{n} = \hat{\boldsymbol{z}}^*$ (see (2.17)). Here, the colour variation of the streamlines (from red to blue) represents the linear variation of the basic density, and $\boldsymbol{B}_0$ denotes the basic (constant) magnetic field.

The first direct numerical simulations of homogeneous hydrodynamical turbulence due to precession were performed in Barker (2016*b*), and there were also earlier simulations with stress-free impermeable walls in Mason & Kerswell (2002). The direct numerical simulations studies indicate a saturation of the precessional instability due to the nonlinear interactions and the development of both 3-D waves with embedded 2-D vortices (see, e.g. Khlifi *et al.* 2018; Pizzi *et al.* 2022). Note that the columnar vortices are commonly found in turbulence subjected to rapid rotation, and would be expected to correspond with zonal flows (Barker 2016*b*). However, in precessing magnetohydrodynamic (MHD) turbulence, the formation of the vortices is inhibited even for a weak background magnetic field (see, e.g. Barker, 2016*a*; Salhi, Khlifi & Cambon 2019). It is worth noting that the latter study extends that of Salhi, Lehner & Cambon (2010) which deals with a linear stability analysis of an unbounded precessing magnetized flow subjected to a background magnetic field, similarly to the Floquet analysis of Lebovitz & Zweibel (2004) (hereafter LZ04) for unbounded elliptical magnetized flow.

In the context of the Earth's magnetic field generation, i.e. the dynamo effect in the liquid outer core (see, e.g. Braginsky 1991), Tilgner (1999) studied MHD flow

https://doi.org/10.1017/jfm.2025.10881 Published online by Cambridge University Press

in precessing spherical shells with and without an imposed magnetic dipole field. He showed that, when a magnetic dipole field with its dipole oriented along the rotation axis of the shell is applied, shear zones develop additional structure and change position and orientation (with respect to the case without a magnetic dipole). Note that several numerical simulations of precession driven dynamos have been performed in order to study the feasibility of dynamo action, as well as the existence of magnetic dipole reversals. In these studies, the incompressible MHD equations (see § 2) have been simulated with a non-zero initial magnetic energy (see, e.g. Cébron *et al.* 2019; Etchevest, Fontana & Dmitruk 2022).

As for the effects of stable density stratification on the precessing flow, Wei & Tilgner (2013) carried out a numerical calculation of the flow driven by both convection and precession in a rotating spherical shell. They found that a stable stratification suppresses possible precessional instabilities, whereas an unstable stratification can lead to both stabilization and destabilization, depending on the parameters such as Ekman, Nusselt, Rayleigh and Poincaré numbers (see, e.g. Wei 2016; Vormann & Hansen 2020).

The effect of an axial stable density stratification on Taylor columns has been previously investigated experimentally and theoretically (see, e.g. Davies 1972; Caton, Janiaud & Hopfinger 2000; Hollerbach & Cally 2009). Benkacem *et al.* (2022) extended Mahalov's theoretical study for precessing 'infinite' Taylor columns (see the solution (1.2)) by including the effect of stratification: they implemented a correction to the basic buoyancy scalar field (see § 2). They showed that stable stratification acts in such a way as to make the subharmonic instability less efficient, so as it disappears for $N \geqslant 0.5\Omega_0$ where N is the Brunt–Väisälä frequency (defined in § 2). Similarly, in the case of unbounded strained-vortex flow with stable axial stratification studied by Miyazaki & Fukumoto (1992), the growth rates for the elliptical instability were invariably reduced: the subharmonic elliptical instability is completely suppressed when $N \geqslant \Omega_0$ (see also Kerswell 2002).

The outline of the paper is structured as follows. The Boussinesq MHD equations as well as the solution for the unperturbed fields (velocity, magnetic field and density) are presented in § 2. The perturbed system in physical space and its counterpart in Fourier space are presented in § 3. The use of the magnetic induction potential scalar (MIPS) (i.e. the inner product of the buoyancy gradient by the magnetic field, (see, Salhi *et al.* 2012)) which is an inviscid invariant, allows us to obtain a four-dimensional Floquet system. In § 4, the stability analysis of the Floquet system is addressed and asymptotic formulae for the maximal growth rate of the subharmonic instabilities are deduced. In § 5, a selection of numerical results is presented and compared with asymptotic formulae. The effect of diffusion is briefly addressed in the special case where the diffusion coefficients (kinetic, thermal and magnetic) are equal. Conclusions and perspectives are offered in § 6.

2. Mathematical formulation

2.1. *The Boussinesq MHD equations*

The Boussinesq approximation ignores density differences except where they appear in terms multiplied by the acceleration due to the buoyancy force (see, e.g. Spiegel & Veronis 1960; Salhi *et al.* 2013). Accordingly, the continuity equation reduces to $\boldsymbol{\nabla}\cdot\tilde{\boldsymbol{u}} = 0$ as for an incompressible fluid.

In a frame rotating uniformly about a fixed axis at the rate $\boldsymbol{\Omega}_p$, the Boussinesq MHD equations for the instantaneous velocity field $\tilde{\boldsymbol{u}}(\boldsymbol{x}, t)$, magnetic field $\tilde{\boldsymbol{b}}(\boldsymbol{x}, t)$ and buoyancy scalar $\tilde{\vartheta}(\boldsymbol{x}, t)$ can be written as (see, e.g. Davidson 2013)

https://doi.org/10.1017/jfm.2025.10881 Published online by Cambridge University Press

$$(\partial_t + \tilde{\boldsymbol{u}}\cdot\boldsymbol{\nabla})\tilde{\boldsymbol{u}} = -\boldsymbol{\nabla}\tilde{p} - 2\boldsymbol{\Omega}_p \times \tilde{\boldsymbol{u}} + \big(\tilde{\boldsymbol{b}}\cdot\boldsymbol{\nabla}\big)\tilde{\boldsymbol{b}} + \tilde{\vartheta}\boldsymbol{n} + \nu\nabla^2\tilde{\boldsymbol{u}}, \tag{2.1a}$$

$$(\partial_t + \tilde{\boldsymbol{u}}\cdot\boldsymbol{\nabla})\,\tilde{\boldsymbol{b}} = \big(\tilde{\boldsymbol{b}}\cdot\boldsymbol{\nabla}\big)\tilde{\boldsymbol{u}} + \eta\nabla^2\tilde{\boldsymbol{b}}, \tag{2.1b}$$

$$(\partial_t + \tilde{\boldsymbol{u}}\cdot\boldsymbol{\nabla})\tilde{\vartheta} = \kappa\nabla^2\tilde{\vartheta}, \tag{2.1c}$$

$$\boldsymbol{\nabla}\cdot\tilde{\boldsymbol{u}} = 0, \tag{2.1d}$$

$$\boldsymbol{\nabla}\cdot\tilde{\boldsymbol{b}} = 0. \tag{2.1e}$$

Here, the magnetic field is scaled using Alfvén velocity units: it is divided by $\sqrt{\rho_0\mu_0}$ where ρ_0 and μ_0 are the constant density and the magnetic permeability of the fluid, $\tilde{p}$ being the total pressure (including the centrifugal potential and the magnetic part) divided by the constant density ρ_0, and $\boldsymbol{\Omega}_p$ is the rotation vector of the reference frame which is constant and ν, η and κ are positive constants that denote the kinematic viscosity, magnetic diffusivity and thermal diffusivity, respectively, and $\boldsymbol{n}$ is a unit vector that aligns with the basic buoyancy scalar gradient. As indicated by an anonymous referee, the natural systems possess a non-negligible adiabatic gradient, sometimes very strong (unlike in experimental situations), and hence, $\tilde{\vartheta}$ should be really defined as an excess over the adiabatic profile (influencing also the basic pressure field), so that the equations indeed look like (2.1).

The equation for the absolute vorticity vector, $\tilde{\boldsymbol{w}} = \boldsymbol{\nabla}\times\tilde{\boldsymbol{u}} + 2\boldsymbol{\Omega}_p$, is obtained by taking the curl of the momentum equation

$$\partial_t\tilde{\boldsymbol{w}} = \boldsymbol{\nabla}\times\big(\tilde{\boldsymbol{u}}\times\tilde{\boldsymbol{w}} + \tilde{\boldsymbol{j}}\times\tilde{\boldsymbol{b}}\big) + \boldsymbol{\nabla}\tilde{\vartheta}\times\boldsymbol{n} + \nu\nabla^2\tilde{\boldsymbol{w}}, \tag{2.2}$$

where $\tilde{\boldsymbol{j}} = \boldsymbol{\nabla}\times\tilde{\boldsymbol{b}}$ is the normalized current density. In addition, we report here the equation for the gradient of the buoyancy scalar,

$$(\partial_t + \tilde{\boldsymbol{u}}\cdot\boldsymbol{\nabla})\,\big(\boldsymbol{\nabla}\tilde{\vartheta}\big) = -\big(\boldsymbol{\nabla}\tilde{\boldsymbol{u}}\big)^T\cdot\big(\boldsymbol{\nabla}\tilde{\vartheta}\big) + \kappa\nabla^2\big(\boldsymbol{\nabla}\tilde{\vartheta}\big), \tag{2.3}$$

where T denotes the transpose. Accordingly, from (2.2) and (2.3) we deduce the equation for the potential vorticity, $\tilde{\Pi}_\kappa = \tilde{\boldsymbol{w}}\cdot\boldsymbol{\nabla}\tilde{\vartheta}$, which is very useful as an invariant in stratified geophysical flows (see, e.g. Pedlosky 2013),

$$(\partial_t + \tilde{\boldsymbol{u}}\cdot\boldsymbol{\nabla})\tilde{\Pi}_\kappa = \big(\boldsymbol{\nabla}\tilde{\vartheta}\big)\cdot\big(\boldsymbol{\nabla}\times\big(\tilde{\boldsymbol{j}}\times\tilde{\boldsymbol{b}}\big)\big) + \nu\big(\boldsymbol{\nabla}\tilde{\vartheta}\big)\cdot\nabla^2\tilde{\boldsymbol{w}} + \kappa\tilde{\boldsymbol{w}}\cdot\nabla^2\big(\boldsymbol{\nabla}\tilde{\vartheta}\big). \tag{2.4}$$

It follows that, in the case of a magnetized Boussinesq ideal fluid, $\tilde{\Pi}_\kappa$ is not a Lagrangian invariant: while it removes the baroclinic torque, it does not remove the Lorentz torque. In contrast, the so-called MIPS, $\tilde{\Pi}_m = \tilde{\boldsymbol{b}}\cdot\boldsymbol{\nabla}\tilde{\vartheta}$ (see, Salhi *et al.* 2012), which is a solution of the following transport equation:

$$(\partial_t + \tilde{\boldsymbol{u}}\cdot\boldsymbol{\nabla})\tilde{\Pi}_m = \eta\big(\boldsymbol{\nabla}\tilde{\vartheta}\big)\cdot\nabla^2\tilde{\boldsymbol{b}} + \kappa\tilde{\boldsymbol{b}}\cdot\nabla^2\big(\boldsymbol{\nabla}\tilde{\vartheta}\big), \tag{2.5}$$

deduced from (2.1*b*) and (2.3), is a Lagrangian invariant for a magnetized Boussinesq ideal fluid. As will be shown later, the use of the magnetic invariant (i.e. MIPS) makes it possible to reduce the linear system of ordinary differential equations, which represents a Floquet problem of the inviscid stability problem, from a five-dimensional system to a four-dimensional one only.

2.2. *The unperturbed system*

The solutions of system (2.1) and (2.2) are conveniently decomposed into a 'basic flow' ($\boldsymbol{U}$, P, $\boldsymbol{W}$, $\boldsymbol{B}$, Θ) and a 'disturbance' ($\boldsymbol{u}$, p, $\boldsymbol{w}$, $\boldsymbol{b}$, ϑ) as

$$\tilde{\boldsymbol{u}} = \boldsymbol{U} + \boldsymbol{u}, \quad \tilde{p} = P + p, \quad \tilde{\boldsymbol{w}} = \boldsymbol{W} + \boldsymbol{w}, \quad \tilde{\boldsymbol{b}} = \boldsymbol{B}_0 + \boldsymbol{b}, \quad \tilde{\vartheta} = \Theta + \vartheta, \tag{2.6}$$

https://doi.org/10.1017/jfm.2025.10881 Published online by Cambridge University Press

where the basic flow is a solution of system (2.1). As indicated in § 1, we consider the unbounded basic flows KBF and MBF given by (1.1) and (1.3), respectively, that can be thought to represent a small patch of a stratified precessing magnetized flow subject to a background magnetic field.

To discuss the admissibility conditions, i.e. the basic flow must be a solution of the system (2.1) (see, Craik 1989), it is convenient to consider the equation for the basic absolute vorticity (2.2), the induction (2.1*b*) and the equation for the basic buoyancy scalar gradient (2.3) supplemented by (2.1*d*, *e*),

$$(\partial_t + \boldsymbol{U}\cdot\boldsymbol{\nabla})\boldsymbol{W} = \boldsymbol{W}\cdot\boldsymbol{\nabla}\boldsymbol{U} + \boldsymbol{\nabla}\times((\boldsymbol{B}_0\cdot\boldsymbol{\nabla})\boldsymbol{B}_0) + \nu\boldsymbol{\nabla}^2\boldsymbol{W}, \tag{2.7a}$$

$$(\partial_t + \boldsymbol{U}\cdot\boldsymbol{\nabla})\boldsymbol{B}_0 = \boldsymbol{B}_0\cdot\boldsymbol{\nabla}\boldsymbol{U} + \eta\boldsymbol{\nabla}^2\boldsymbol{B}_0, \tag{2.7b}$$

$$(\partial_t + \boldsymbol{U}\cdot\boldsymbol{\nabla})(\boldsymbol{\nabla}\Theta) = -(\boldsymbol{\nabla}\Theta)\cdot\boldsymbol{\nabla}(\boldsymbol{U})^T + \kappa\boldsymbol{\nabla}^2(\boldsymbol{\nabla}\Theta), \tag{2.7c}$$

with $\boldsymbol{\nabla}\cdot\boldsymbol{U} = 0$ and $\boldsymbol{\nabla}\cdot\boldsymbol{B}_0 = 0$. Recall that the unit vector $\boldsymbol{n}$ aligns with the basic buoyancy scalar gradient, so that, $\boldsymbol{\nabla}\Theta\times\boldsymbol{n} = \boldsymbol{0}$.

2.2.1. *Basic velocity*

Recall that the KBF, i.e. the velocity field of the precessing flow described by (1.1), approximates the laminar Poincaré flow far from the boundaries of a spheroid if $\varepsilon \ll 1$, and the tidal deformation is neglected (see, Poincaré 1910; Kerswell 1993; Salhi & Cambon 2009). In this case, the basic absolute vorticity vector, $\boldsymbol{W} = \boldsymbol{\nabla}\times\boldsymbol{U} + 2\Omega_p = 2\Omega_0(2\varepsilon\hat{\boldsymbol{x}} + \hat{\boldsymbol{z}})$, does not align with the solid body rotation. In counterpart, the MBF, i.e. the velocity field of the precessing flow described by (1.3), characterizes an infinite column in which a tilted (sheared) streamline solution can exist under precession (see, Mahalov 1993; Salhi & Cambon 2009). In this case, $\boldsymbol{W} = 2\Omega_0\hat{\boldsymbol{z}}$ aligns with the solid body rotation.

Accordingly, in the pure hydrodynamic case, so that $\boldsymbol{B}_0$ and $\boldsymbol{\nabla}\Theta$ are zero, both KBF and MBF are exact solutions of (2.7*a*). Note that, the main difference between these two base flows is the cross-gradient direction of the plane shear: for the KBF it is along $\hat{\boldsymbol{y}}$ and varies linearly with respect to the vertical space coordinate z, while for the MBF it is along the vertical axis $\hat{\boldsymbol{z}}$ and varies linearly with respect to the horizontal space coordinate y. Note that the trajectory of a fluid particle can be determined by resolving the equation $d_t\boldsymbol{x} = \boldsymbol{\nabla}\boldsymbol{U}\cdot\boldsymbol{x}$. Accordingly, for the KBF, for example, we find

$$x(\tau) = x_0\cos\tau - y_0\sin\tau,\ \ y(\tau) = x_0\sin\tau + y_0\cos\tau,\ \ z(\tau) = z_0 + 2\varepsilon(x - x_0), \tag{2.8}$$

where $\tau = \Omega_0 t$ is a dimensionless time and $\boldsymbol{x}_0 = (x_0,\, y_0,\, z_0)^T$ is the initial (at $t = 0$) vector position. It follows that the fluid particle describes an ellipse in the $(x^*,\, y^*)$-plane,

$$\boldsymbol{x} = x\hat{\boldsymbol{x}} + y\hat{\boldsymbol{y}} + z\hat{\boldsymbol{z}} = x^*\hat{\boldsymbol{x}}^* + y^*\hat{\boldsymbol{y}}^* + z^*\hat{\boldsymbol{z}}^*, \tag{2.9a}$$

$$x^* = \frac{1}{\sqrt{1+4\varepsilon^2}}(x + 2\varepsilon z), \quad y^* = y, \quad z^* = \frac{1}{\sqrt{1+4\varepsilon^2}}(-2\varepsilon x + z). \tag{2.9b}$$

Indeed, one easily verifies that z^* (given by (2.9*b*)) is time-independent and

$$\frac{1}{\sqrt{1+4\varepsilon^2}}\left(x^* - 2\varepsilon z^*\right)^2 + y^{*2} = \text{const.} \tag{2.10}$$

On the other hand, we also note that in some previous studies (see, Mason & Kerswell 2002; Barker 2016*b*; Pizzi *et al.* 2022) the 'mantle frame' has been used: this consists in applying the following transformation to the solution (1.1):

$$x_1 = x\cos t + y\sin t, \quad x_2 = -x\sin t + y\cos t, \quad x_3 = z. \tag{2.11}$$

https://doi.org/10.1017/jfm.2025.10881 Published online by Cambridge University Press

2.2.2. *Basic magnetic field and buoyancy scalar*

Given the solutions (1.1) and (1.3), a constant basic magnetic field $\boldsymbol{B}_0$, which is a trivial solution of (2.7*a*), must also satisfy (2.7*b*), so that, $\boldsymbol{B}_0\cdot\boldsymbol{\nabla U}=0$, and hence, $\boldsymbol{B}_0$ aligns with the basic absolute vorticity:

$$\boldsymbol{B}_0 = B_0\big(2\varepsilon\hat{\boldsymbol{x}}+\hat{\boldsymbol{z}}\big) \quad \text{for the KBF,} \tag{2.12a}$$

$$\boldsymbol{B}_0 = B_0\hat{\boldsymbol{z}} \quad \text{for the MBF.} \tag{2.12b}$$

Here, B_0 is a positive constant.

Given the above solutions for $(\boldsymbol{U},\,\boldsymbol{B}_0)$, in a stratified MHD case under the Boussinesq approximation the basic buoyancy scalar must be a solution of the (2.7*c*).

For the KBF (given by (1.1)), a vertical constant basic density gradient, $\boldsymbol{\nabla}\varrho=(\mathrm{d}\varrho/\mathrm{d}z)\hat{\boldsymbol{z}}$, so that

$$\Theta = -\frac{g}{\rho_0}\left(\frac{\mathrm{d}\varrho}{\mathrm{d}z}\right)z = N^2 z, \quad N^2=-\frac{g}{\rho_0}\frac{\mathrm{d}\varrho}{\mathrm{d}z}, \quad \boldsymbol{n}=\frac{\boldsymbol{\nabla}\Theta}{\|\boldsymbol{\nabla}\Theta\|}=\hat{\boldsymbol{z}} \tag{2.13}$$

is an admissible solution. Here N being the Brunt–Väisälä frequency ($N^2>0$ for a stable stratification).

For the MBF (given by (1.3)), we consider that, *a priori*, the basic buoyancy scalar varies linearly with the space coordinates (see, e.g. Craik 1989), $\Theta=(\partial_x\Theta)x+(\partial_y\Theta)y+N^2\boldsymbol{z}$, so that, without precession, it reduces to $\Theta=N^2\boldsymbol{z}$. By substituting the above form into (2.7*c*), we obtain, $(\boldsymbol{\nabla U})^T\cdot(\boldsymbol{\nabla}\Theta)=\boldsymbol{0}$,

$$\begin{pmatrix}0&1&0\\-1&0&-2\varepsilon\\0&0&0\end{pmatrix}\cdot\begin{pmatrix}\partial_x\Theta\\\partial_y\Theta\\N^2\end{pmatrix}=\begin{pmatrix}0\\0\\0\end{pmatrix} \tag{2.14}$$

or equivalently,

$$\partial_y\Theta=0 \quad \text{and} \quad \partial_x\Theta=-2\varepsilon N^2. \tag{2.15}$$

Accordingly, the basic buoyancy scalar takes the form

$$\Theta(\boldsymbol{x})=N^2(-2\varepsilon x+z), \quad \boldsymbol{n}=\frac{\boldsymbol{\nabla}\Theta}{\|\boldsymbol{\nabla}\Theta\|}=\frac{1}{\sqrt{1+4\varepsilon^2}}\big(-2\varepsilon\hat{\boldsymbol{x}}+\hat{\boldsymbol{z}}\big). \tag{2.16}$$

The presence of the additional horizontal component of the basic buoyancy scalar, which vanishes in the case without precession ($\varepsilon=0$), is thereby due to the gyroscopic torque as for the additional mean shear. In a cylindrical coordinate system $(r,\,\varphi,\,z)$ the solution (2.16) can be rewritten as

$$\Theta(\boldsymbol{x})=N^2(-2\varepsilon\,(\cos\varphi)r+z), \quad \boldsymbol{n}=\frac{1}{\sqrt{1+4\varepsilon^2}}\big[-2\varepsilon\,\big((\cos\varphi)\hat{\boldsymbol{r}}-(\sin\varphi)\hat{\boldsymbol{\varphi}}\big)+\hat{\boldsymbol{z}}\big]. \tag{2.17}$$

Thus, we recover the solution proposed by Benkacem *et al.* (2022) who extended Mahalov's theoretical study (Mahalov 1993) by taking into account the effect of stable stratification on precessing columns: they proposed a first-order correction to the profile of the basic buoyancy scalar because the Coriolis force alters the base flow (see their Appendix A).

For the sake of clarity, we repeat here the base flows considered in the present study,

$$\boldsymbol{\nabla U}=\Omega_0\begin{pmatrix}0&-1&0\\1&0&-2\varepsilon\\0&0&0\end{pmatrix},\ \boldsymbol{\Omega}_p=\Omega_0\begin{pmatrix}\varepsilon\\0\\0\end{pmatrix},\ \boldsymbol{B}_0=B_0\begin{pmatrix}2\varepsilon\\0\\1\end{pmatrix},\ \boldsymbol{\nabla}\Theta=N^2\begin{pmatrix}0\\0\\1\end{pmatrix}, \tag{2.18}$$

https://doi.org/10.1017/jfm.2025.10881 Published online by Cambridge University Press

for the KBF and

$$\boldsymbol{\nabla U} = \Omega_0 \begin{pmatrix} 0 & -1 & 0 \\ 1 & 0 & 0 \\ 0 & -2\varepsilon & 0 \end{pmatrix}, \ \boldsymbol{\Omega}_p = \Omega_0 \begin{pmatrix} \varepsilon \\ 0 \\ 0 \end{pmatrix}, \ \boldsymbol{B}_0 = B_0 \begin{pmatrix} 0 \\ 0 \\ 1 \end{pmatrix}, \ \boldsymbol{\nabla}\Theta = N^2 \begin{pmatrix} -2\varepsilon \\ 0 \\ 1 \end{pmatrix}, \quad (2.19)$$

for the MBF.

3. Perturbed system

In the following, we consider the case of a non-diffusive fluid. Diffusivity effects with the assumption that the diffusion coefficients are equal ($\nu = \eta = \kappa$) or, equivalently, the magnetic and thermal Prandtl numbers are equal to one are briefly discussed at the end of § 5.

3.1. *Linearized system in physical space*

We substitute the solutions (2.6) into the system (2.1) and linearize. The resulting perturbed equations are

$$(\partial_t + \boldsymbol{U}\cdot\boldsymbol{\nabla})\boldsymbol{u} = -\boldsymbol{\nabla} p - \boldsymbol{u}\cdot\boldsymbol{\nabla U} - 2\varepsilon\Omega_0\hat{\boldsymbol{x}}\times\boldsymbol{u} + (\boldsymbol{B}_0\cdot\boldsymbol{\nabla})\boldsymbol{b} + \vartheta\boldsymbol{n}, \quad (3.1a)$$

$$(\partial_t + \boldsymbol{U}\cdot\boldsymbol{\nabla})\boldsymbol{b} = \boldsymbol{b}\cdot\boldsymbol{\nabla U} + (\boldsymbol{B}_0\cdot\boldsymbol{\nabla})\boldsymbol{u}, \quad (3.1b)$$

$$(\partial_t + \boldsymbol{U}\cdot\boldsymbol{\nabla})\vartheta = -\boldsymbol{u}\cdot\boldsymbol{\nabla}\Theta, \quad (3.1c)$$

$$\boldsymbol{\nabla}\cdot\boldsymbol{u} = 0, \quad (3.1d)$$

$$\boldsymbol{\nabla}\cdot\boldsymbol{b} = 0. \quad (3.1e)$$

For an inviscid and non-diffusive Boussinesq fluid, the potential induction magnetic scalar (MIPS) $\tilde{\Pi}_m = \Pi_m + \varpi_m + \varpi_m^{(nl)}$ is a Lagrangian invariant, as already indicated (see (2.5)), and its linear part takes the form

$$\varpi_m = \boldsymbol{b}\cdot\boldsymbol{\nabla}\Theta + \boldsymbol{B}_0\cdot\boldsymbol{\nabla}\vartheta \quad (3.2)$$

while $\varpi_m^{(nl)} = \boldsymbol{b}\cdot\boldsymbol{\nabla}\vartheta$ denotes its nonlinear part which is omitted in the present study.

3.2. *Floquet system in wave space*

The disturbances are expressed in terms of plane waves, for which the direction and the speed of propagation depend on time (see, Bayly 1986; Craik & Criminale 1986),

$$\left(\boldsymbol{u},\, p,\, \boldsymbol{b},\, N^{-1}\vartheta\right)(\boldsymbol{x},\, t) = \left(\hat{\boldsymbol{u}},\, \hat{p},\, \hat{\boldsymbol{b}},\, \hat{\vartheta}\right)(\boldsymbol{k},\, t)\exp(\mathrm{i}\boldsymbol{k}(t)\cdot\boldsymbol{x}) \quad (3.3)$$

where $\mathrm{i}^2 = -1$, $\boldsymbol{k}(t)$ is the wavevector and $\hat{\vartheta}(\boldsymbol{k})$ has a dimension of a velocity. Accordingly, the material derivative of the fluctuating velocity $\boldsymbol{u}$ can be rewritten as

$$(\partial_t + \boldsymbol{U}\cdot\boldsymbol{\nabla})\boldsymbol{u}(\boldsymbol{x},\, t) = \left[\partial_t\hat{\boldsymbol{u}} + \mathrm{i}\left(\left(d_t\boldsymbol{k} + (\boldsymbol{\nabla U})^T\cdot\boldsymbol{k}\right)\cdot\boldsymbol{x}\right)\hat{\boldsymbol{u}}\right]\exp(\mathrm{i}\boldsymbol{k}(t)\cdot\boldsymbol{x}). \quad (3.4)$$

To remove the explicit dependence on $\boldsymbol{x}$ in the resulting equations for the Fourier amplitudes $\hat{\boldsymbol{u}}$, $\hat{\boldsymbol{b}}$ and $\hat{\vartheta}$ one has to ensure that $\boldsymbol{k}(t)$ varies in time according to the eikonal equation (see, Bayly 1986; Craik & Criminale 1986),

$$d_t\boldsymbol{k} = -(\boldsymbol{\nabla U})^T\cdot\boldsymbol{k} \quad (3.5)$$

where $d_t(\cdot) \equiv d(\cdot)/\mathrm{d}t$.

https://doi.org/10.1017/jfm.2025.10881 Published online by Cambridge University Press

Substituting the plane waves solution (3.3) into the system (3.1) and taking into account the eikonal (3.5), we obtain

$$d_t\hat{\boldsymbol{u}} = -\mathrm{i}\hat{p}\boldsymbol{k} - \hat{\boldsymbol{u}}\cdot\boldsymbol{\nabla}\boldsymbol{U} - 2\varepsilon\Omega_0\hat{\boldsymbol{x}}\times\hat{\boldsymbol{u}} + \mathrm{i}(\boldsymbol{k}\cdot\boldsymbol{B}_0)\hat{\boldsymbol{b}} + N\hat{\vartheta}\boldsymbol{n}, \tag{3.6a}$$

$$d_t\hat{\boldsymbol{b}} = \hat{\boldsymbol{b}}\cdot\boldsymbol{\nabla}\boldsymbol{U} + \mathrm{i}(\boldsymbol{k}\cdot\boldsymbol{B}_0)\hat{\boldsymbol{u}}, \tag{3.6b}$$

$$d_t\hat{\vartheta} = -N^{-1}\hat{\boldsymbol{u}}\cdot\boldsymbol{\nabla}\Theta, \tag{3.6c}$$

together with $\boldsymbol{k}\cdot\hat{\boldsymbol{u}} = 0$ and $\boldsymbol{k}\cdot\hat{\boldsymbol{b}} = 0$. The use of the latter conditions allows one to eliminate the Fourier amplitude of fluctuating pressure,

$$\hat{p} = \mathrm{i}k^{-2}\left(\left(\hat{\boldsymbol{u}}\cdot\boldsymbol{\nabla}\boldsymbol{U}\right)\cdot\boldsymbol{k} + \left((\boldsymbol{\nabla}\boldsymbol{U})^T\cdot\boldsymbol{k}\right)\cdot\hat{\boldsymbol{u}} + 2\varepsilon\Omega_0\left(\hat{\boldsymbol{x}}\times\hat{\boldsymbol{u}}\right)\cdot\boldsymbol{k} - N\left(\boldsymbol{n}\cdot\boldsymbol{k}\right)\hat{\vartheta}\right) \tag{3.7}$$

and to reduce the above seven-component Floquet system to a five-component version, where $k = \|\boldsymbol{k}\|$. The spectral counterpart of the linear part of MIPS given by (3.2) reads

$$\hat{\varpi}_m = \hat{\boldsymbol{b}}\cdot\boldsymbol{\nabla}\Theta + \mathrm{i}(\boldsymbol{k}\cdot\boldsymbol{B}_0)\hat{\vartheta} = \text{const.} \tag{3.8}$$

It will be used to reduce the five-dimensional Floquet system to a inhomogeneous four-dimensional Floquet system.

3.3. *The KBF case*

The developments presented in this section as well as those presented in § 3.4 concern the KBF. Those which concern the MBF are reported in Appendix A for greater clarity for the reader.

3.3.1. *Time-periodic wavevector*

For the KBF (described by (2.18)), (3.5) reduces to

$$d_t k_1 = -\Omega_0 k_2, \quad d_t k_2 = \Omega_0 k_1, \quad d_t k_3 = 2\varepsilon\Omega_0 k_2 = -2\varepsilon d_t k_1, \tag{3.9}$$

so that

$$d_t k^2 = d_t\left(k_1^2 + k_2^2 + k_3^2\right) = 4\Omega_0\varepsilon k_2 k_3, \tag{3.10}$$

where $k = \|\boldsymbol{k}\|$. Equation (3.9) can be solved to give

$$k_1 = k_p\cos(\tau - \phi), \quad k_2 = k_p\sin(\tau - \phi), \quad k_3 = k_0 - 2\varepsilon k_1, \tag{3.11}$$

where $\tau = \Omega_0 t$ is a dimensionless time, $\tan\phi = -k_{20}/k_{10}$ and

$$k_p = \sqrt{k_1^2 + k_2^2} = \sqrt{k_{10}^2 + k_{20}^2}, \quad k_0 = k_{30} + 2\varepsilon k_{10} = k_3 + 2\varepsilon k_1, \tag{3.12}$$

in which $\boldsymbol{K}_0 = (k_{10}, k_{20}, k_{30})^T$ is the initial wavevector. Both k_p and k_0 are time-independent.

For purposes of studying stability, we may set $\phi = 0$. This is easily seen by making the substitution $\Omega_0 t' = \Omega_0 t - \phi$, which eliminates ϕ from the equation.

3.3.2. *One-dimensional two component and 2-D three component flow cases*

For $k_p = 0$, so that $k_1 = k_2 = 0$: the wavevector aligns with the vertical unit vector $\hat{\boldsymbol{z}}$, $\boldsymbol{k} = k_3\hat{\boldsymbol{z}} = k_{30}\hat{\boldsymbol{z}}$. In this case, the constraints $\boldsymbol{k}\cdot\hat{\boldsymbol{u}} = 0$ and $\boldsymbol{k}\cdot\hat{\boldsymbol{b}} = 0$ give $\hat{u}_3 = 0$ and $\hat{b}_3 = 0$, respectively. Thus, this flow configuration corresponds to one-dimensional two component (1D2C) flows. System (3.6) reduces to a four-dimensional system for the velocity and magnetic field horizontal fluctuations which are not affected by the effect of stratification

https://doi.org/10.1017/jfm.2025.10881 Published online by Cambridge University Press

(at least for the linear regime, i.e. the nonlinear interactions are omitted),

$$d_t \begin{pmatrix} \hat{u}_1 \\ \hat{u}_2 \\ \hat{b}_1 \\ \hat{b}_2 \end{pmatrix} = \begin{pmatrix} 0 & \Omega_0 & \mathrm{i}k_3 B_0 & 0 \\ -\Omega_0 & 0 & 0 & \mathrm{i}k_3 B_0 \\ \mathrm{i}k_3 B_0 & 0 & 0 & -\Omega_0 \\ 0 & \mathrm{i}k_3 B_0 & \Omega_0 & 0 \end{pmatrix} \cdot \begin{pmatrix} \hat{u}_1 \\ \hat{u}_2 \\ \hat{b}_1 \\ \hat{b}_2 \end{pmatrix} \tag{3.13}$$

with $\hat{\vartheta} = \text{const.}$, in agreement with (3.8). It is not difficult to show that there can be no instability associated with the solution of the above differential system.

For the case where $k_0 = 0$, so that $k_3 = -2\varepsilon k_1$ and $\boldsymbol{k} = k_1(\hat{\boldsymbol{x}} - 2\varepsilon\hat{\boldsymbol{z}}) + k_2\hat{\boldsymbol{y}}$, and the constraints $\boldsymbol{k}\cdot\hat{\boldsymbol{u}} = 0$ and $\boldsymbol{k}\cdot\hat{\boldsymbol{b}} = 0$ reduce to

$$k_1\big(\hat{u}_1 + 2\varepsilon\hat{u}_3\big) + k_2\hat{u}_2 = 0, \quad k_1\big(\hat{b}_1 + 2\varepsilon\hat{b}_3\big) + k_2\hat{b}_2 = 0. \tag{3.14}$$

Moreover, in the linear regime, there is no effect of the basic magnetic field on the velocity and density fluctuations. The magnetic field fluctuations behave like a passive field in a precessing stratified flow, since the system (3.1) reduces to

$$d_t\hat{\boldsymbol{u}} = -\mathrm{i}\hat{p}\boldsymbol{k} - \hat{\boldsymbol{u}}\cdot\boldsymbol{\nabla}\boldsymbol{U} - 2\varepsilon\Omega_0\hat{\boldsymbol{x}}\times\hat{\boldsymbol{u}} + N\hat{\vartheta}\boldsymbol{n}, \tag{3.15a}$$

$$d_t\hat{\boldsymbol{b}} = \hat{\boldsymbol{b}}\cdot\boldsymbol{\nabla}\boldsymbol{U}, \tag{3.15b}$$

$$d_t\hat{\vartheta} = -N^{-1}\hat{\boldsymbol{u}}\cdot\boldsymbol{\nabla}\Theta, \tag{3.15c}$$

or equivalently,

$$\hat{\omega}_3 = \text{const.}, \quad \hat{b}_3 = \text{const.}, \quad k_1\hat{b}_2 - k_2\hat{b}_1 + 2\varepsilon k_2\hat{b}_3 = \text{const.}, \tag{3.16a}$$

$$d_\tau\hat{\psi} = -2\mathrm{i}\varepsilon k_1\hat{\omega}_3 + (N/\Omega_0)\,k_p^2\hat{\vartheta}, \tag{3.16b}$$

$$d_\tau\vartheta = -(N/\Omega_0)\hat{u}_3, \tag{3.16c}$$

where $\hat{\psi} = k^2\hat{u}_3$, $k^2 = k_p^2 + k_3^2 = k_p^2 + 4\varepsilon^2k_1^2 = k_p^2(1 + 4\varepsilon^2\cos^2\tau)$ and $\hat{\omega}_3 \equiv \mathrm{i}(k_1\hat{u}_2 - k_2\hat{u}_1)$ denotes the Fourier amplitude of the vertical vorticity component ($\boldsymbol{\omega} = \boldsymbol{\nabla}\times\boldsymbol{u}$). Accordingly, we deduce the following inhomogeneous second-order differential equation (i.e. a Hill's equation):

$$d_{\tau\tau}\hat{\psi} + (N/\Omega_0)^2\big(1 + 2\varepsilon^2(1 + 2\cos 2\tau)\big)\hat{\psi} = -2\varepsilon k_p\hat{\omega}_3\sin\tau. \tag{3.17}$$

The stability analysis of (3.17) indicates that there is no instability at order $O(\varepsilon)$. In counterpart, on times cales of order ε^{-2}, the solutions are unstable at and near $N/\Omega_0 = 1$ with a maximal growth rate, $\sigma_m = \varepsilon^2/2$ (more details are given in the Supplementary material).

3.4. *Floquet system for the 3-D three component flow case*

For perturbations with wavenumber $k_0 \neq 0$, we transform the resulting Floquet system in terms of the following variables to facilitate subsequent calculations (see, Salhi *et al.* 2010):

$$\Omega_0\hat{c}_1 = \big(k_1\hat{u}_2 - k_2\hat{u}_1\big) + 2\varepsilon k_2\hat{u}_3, \quad \Omega_0\hat{c}_2 = -k_0\hat{u}_3, \tag{3.18a}$$

$$\Omega_0\hat{c}_3 = \big(k_1\hat{b}_2 - k_2\hat{b}_1\big) + 2\varepsilon k_2\hat{b}_3, \quad \Omega_0\hat{c}_4 = -k_0\hat{b}_3, \quad \Omega_0\hat{c}_5 = -k_0\hat{\vartheta}. \tag{3.18b}$$

Given (3.7), which reduces to

$$\hat{p} = -\mathrm{i}k^{-2}\big(2\Omega_0\big(k_1\hat{u}_2 - k_2\hat{u}_1\big) + 6\varepsilon\Omega_0k_2\hat{u}_3 - 2\varepsilon\Omega_0k_3\hat{u}_2 + k_3N\hat{\vartheta}\big), \tag{3.19}$$

https://doi.org/10.1017/jfm.2025.10881 Published online by Cambridge University Press

we transform the system (3.6) according to these new variables,

$$d_\tau \hat{c}_1 = -4\varepsilon\left(\frac{k_2k_3}{k^2}+\varepsilon\frac{k_1k_2}{k^2}\right)\hat{c}_1 - 2\left(1+\varepsilon\frac{k_1}{k_0}+4\varepsilon^3\frac{k_1k_2^2}{k_0k^2}\right)\hat{c}_2 + \mathrm{i}\mathcal{B}\mu\hat{c}_3 - 2\varepsilon\mathcal{N}\frac{k_2k_p^2}{k_0k^2}\hat{c}_5, \tag{3.20a}$$

$$d_\tau \hat{c}_2 = 2\frac{k_0(k_0-\varepsilon k_1)}{k^2}\hat{c}_1 + 4\varepsilon^2\frac{k_1k_2}{k^2}\hat{c}_2 + \mathrm{i}\mathcal{B}\mu\hat{c}_4 + \mathcal{N}\frac{k_p^2}{k^2}\hat{c}_5, \tag{3.20b}$$

$$d_\tau \hat{c}_3 = \mathrm{i}\mathcal{B}\mu\hat{c}_1, \tag{3.20c}$$

$$d_\tau \hat{c}_4 = \mathrm{i}\mathcal{B}\mu\hat{c}_2, \tag{3.20d}$$

$$d_\tau \hat{c}_5 = -\mathcal{N}\hat{c}_2 \tag{3.20e}$$

where $d_\tau(\cdot) = \Omega_0^{-1} d_t(\cdot)$ and

$$-1 \leqslant \mu = \frac{k_0}{\sqrt{k_p^2+k_0^2}} \leqslant 1, \quad \mathcal{B} = \frac{B_0\sqrt{k_p^2+k_0^2}}{\Omega_0}, \quad \mathcal{N} = \frac{N}{\Omega_0}, \tag{3.21}$$

which are the parameters of the Floquet system in addition to the pression parameter ε. We note that, at small scales, i.e. $\sqrt{k_p^2+k_0^2} \gg 1$, $\mathcal{B}$ is large even if $B_0/\Omega_0 \sim 1$.

On the other hand, combining (3.20*d*) and (3.20*e*), we deduce the following relation:

$$\mathcal{N}\hat{c}_4 + \mathrm{i}\mathcal{B}\mu\hat{c}_5 = -\Omega_0^{-1}k_0\left(N\hat{b}_3 + \mathrm{i}B_0k_0\hat{\vartheta}\right) = -\Omega_0^{-1}k_0\hat{\varpi} = \text{const.}, \tag{3.22}$$

which represents the spectral counterpart of the linear part of MIPS (see (3.8)). Accordingly, system (3.20) can be further reduced to a fourth-order inhomogeneous Floquet system for $\hat{\boldsymbol{c}} = (\hat{c}_1, \hat{c}_2, \hat{c}_3, \hat{c}_4)^T$,

$$d_\tau \hat{\boldsymbol{c}} = \boldsymbol{D}\cdot\hat{\boldsymbol{c}} + \hat{\boldsymbol{\varphi}}, \tag{3.23}$$

where the only non-zero elements of $\boldsymbol{D}(\tau)$ are

$$D_{11} = -4\varepsilon\left(\frac{k_2k_3}{k^2}+\varepsilon\frac{k_1k_2}{k^2}\right), \tag{3.24a}$$

$$D_{12} = -2\left(1+\varepsilon\frac{k_1}{k_0}+4\varepsilon^3\frac{k_1k_2^2}{k_0k^2}\right), \tag{3.24b}$$

$$D_{13} = D_{31} = D_{42} = \mathrm{i}\mathcal{B}\mu, \tag{3.24c}$$

$$D_{14} = -2\mathrm{i}\varepsilon\frac{\mathcal{N}}{\mathcal{B}\mu^2}\frac{k_2k_p^2}{k^3}, \tag{3.24d}$$

$$D_{21} = 2\frac{k_0(k_0-\varepsilon k_1)}{k^2}, \tag{3.24e}$$

$$D_{22} = 4\varepsilon^2\frac{k_1k_2}{k^2}, \tag{3.24f}$$

$$D_{24} = \mathrm{i}\mathcal{B}\mu + \mathrm{i}\frac{\mathcal{N}}{\mathcal{B}\mu}\frac{k_p^2}{k^2}. \tag{3.24g}$$

Therefore, the homogeneous system is

$$d_\tau \hat{\boldsymbol{c}} = \boldsymbol{D}\cdot\hat{\boldsymbol{c}}, \tag{3.25}$$

https://doi.org/10.1017/jfm.2025.10881 Published online by Cambridge University Press

while the non-zero components of the inhomogeneous term in (3.23) take the form

$$\hat{\varphi}_1 = -2\mathrm{i}\varepsilon \frac{N\Omega_0}{B_0}\frac{k_2 k_p^2}{k_0 k^2}\hat{\varpi}_m, \quad \hat{\varphi}_2 = \mathrm{i}\frac{N\Omega_0}{B_0}\frac{k_p^2}{k^2}\hat{\varpi}_m, \tag{3.26}$$

and it can be seen as a time-varying forcing excitation. The linear system (3.23) has the properties $\boldsymbol{D}(\tau + T) = \boldsymbol{D}(\tau)$ and $\hat{\boldsymbol{\varphi}}(\tau + T) = \hat{\boldsymbol{\varphi}}(\tau)$ where $T = 2\pi$ is the period common to both the matrix $\boldsymbol{D}(\tau)$ and the vector $\hat{\boldsymbol{\varphi}}(\tau)$. Floquet theory does not address stability of the inhomogeneous system described by (3.20) where the 'forcing excitation' $\hat{\boldsymbol{\varphi}}(\tau)$ is present. However, the T-periodic nature of $\hat{\boldsymbol{\varphi}}(\tau)$ allows an extension to the theory (see, Slane & Tragesser 2011). By adding a forcing excitation, the general behaviour predicted by Floquet theory for the homogeneous system changed only for the case of semisimple Floquet multipliers that are identically equal to one, i.e. one is the only multiplier on the unit circle and is semisimple. In this case, the presence of the forcing excitation caused the solution to diverge (see, Slane & Tragesser 2011). Incidentally, for several values of the parameters $(\mathcal{B}, \mathcal{N}, \varepsilon, \mu)$, we have numerically determined the stability and instability regions by integrating the 5×5 Floquet system (without involving MIPS, i.e. system (3.20)) as well as the resulting 4×4 Floquet system with $\hat{\varpi}_m = 0$ (i.e. system (3.25)). We obtained the same results for both systems (up to numerical errors). We note that the determinant of the fundamental matrix solution is unity at $\tau = 2\pi$ for both Floquet systems (see (4.3)). This indicates that the neutral case of system (3.25) could be characterized by the fact that unity is not the only multiplier on the unit circle.

3.5. *Resonant cases of MIG waves*

In this section, we start from the case without precession, so that both the background shear and the Coriolis force vanish. In that case, there are MIG waves. The resonant cases of MIG waves have been characterized by SC23 in their study of the MGE instability . Because some resonant cases of MIG waves become destabilizing in stratified magnetized precessing flows ($\varepsilon \neq 0$), we briefly recall here the analysis made by SC23.

We denote by $\boldsymbol{D}_0$ the matrix $\boldsymbol{D}$ for $\varepsilon = 0$ (i.e. circular streamlines)

$$\boldsymbol{D}_0 = \Omega_0 \begin{pmatrix} 0 & -2\Omega_0 & \mathrm{i}\omega_a & 0 \\ (2\Omega_0)^{-1}\omega_r^2 & 0 & 0 & \mathrm{i}\left(\omega_a^2 + \omega_g^2\right)\omega_a^{-1} \\ \mathrm{i}\omega_a & 0 & 0 & 0 \\ 0 & \mathrm{i}\omega_a & 0 & 0 \end{pmatrix} \tag{3.27}$$

where ω_r, ω_a and ω_g are the frequencies of inertial, Alfvén and gravity waves, respectively,

$$\omega_r = \frac{2|\boldsymbol{\Omega}_0 \cdot \boldsymbol{K}_0|}{K_0} = 2\Omega_0|\mu|, \tag{3.28a}$$

$$\omega_a = \boldsymbol{B}_0 \cdot \boldsymbol{K}_0 = B_0 k_0 = B_0 K_0 |\mu|, \tag{3.28b}$$

$$\omega_g = N\frac{\|\hat{\boldsymbol{z}} \times \boldsymbol{K}_0\|}{K_0} = N\sqrt{1-\mu^2}. \tag{3.28c}$$

The eigenvalues σ_j $(j = 1, 2, 3, 4)$ of the constant matrix $\boldsymbol{D}_0$ such that

$$|\boldsymbol{D}_0 - \sigma \boldsymbol{I}_4| = |\boldsymbol{D}_0 - \mathrm{i}\omega \boldsymbol{I}_4| = 0, \tag{3.29}$$

https://doi.org/10.1017/jfm.2025.10881 Published online by Cambridge University Press

where $\boldsymbol{I}_4$ is the four-dimensional unit matrix, take the form

$$-\Omega_0^2\sigma_{1,2}^2=\omega_{1,2}^2=\frac{1}{2}\left[2\omega_a^2+\omega_r^2+\omega_g^2+\sqrt{\left(\omega_r^2+\omega_g^2\right)^2+4\omega_r^2\omega_a^2}\,\right], \tag{3.30a}$$

$$-\Omega_0^2\sigma_{3,4}^2=\omega_{3,4}^2=\frac{1}{2}\left[2\omega_a^2+\omega_r^2+\omega_g^2-\sqrt{\left(\omega_r^2+\omega_g^2\right)^2+4\omega_r^2\omega_a^2}\,\right], \tag{3.30b}$$

or equivalently,

$$\omega_1=-\omega_2=\frac{\Omega_0}{\sqrt{2}}\sqrt{\left(4+2\mathcal{B}^2-\mathcal{N}^2\right)\mu^2+\mathcal{N}^2+\sqrt{\left[\left(4-\mathcal{N}^2\right)\mu^2+\mathcal{N}^2\right]^2+16\mathcal{B}^2\mu^4}}, \tag{3.31a}$$

$$\omega_3=-\omega_4=\frac{\Omega_0}{\sqrt{2}}\sqrt{\left(4+2\mathcal{B}^2-\mathcal{N}^2\right)\mu^2+\mathcal{N}^2-\sqrt{\left[\left(4-\mathcal{N}^2\right)\mu^2+\mathcal{N}^2\right]^2+16\mathcal{B}^2\mu^4}}. \tag{3.31b}$$

Because $\omega_1\geqslant\omega_3$, fast waves have frequency ω_1, while slow waves have frequency ω_3. In the non-magnetized case, fast modes reduce to the purely hydrodynamic modes (i.e. inertia-gravity waves). In counterpart, slow waves are purely magnetic modes because ω_3 reduces to zero for $\mathcal{B}=0$ (see LZ04). The expression of the eigenvectors associated with the eigenvalues σ_1, σ_2, σ_3 and σ_4 is reported in Appendix B.

The resonant cases of MIG waves are those parameter values (μ, $\mathcal{N}$, $\mathcal{B}$,) such that

$$\omega_i-\omega_j=n\Omega_0,\quad (i\neq j). \tag{3.32}$$

As will be shown later, some resonant cases of order $n=1$ are destabilizing, whereas in the case of an elliptical flow the only resonant cases that can lead to instability are those for which the integer n is even (see SC23). Indeed, in the precessing flow case, the components of the wavevector vary in time as $\sim\exp(\pm\mathrm{i}\Omega_0 t)$, reflecting the Ω_0-frequency of the strain field, while in the elliptical flow case they vary as $\sim\exp(\pm2\mathrm{i}\Omega_0 t)$, corresponding to a doubled frequency. This difference directly accounts for the fact that precessing flows can exhibit destabilizing resonances already for $n=1$, whereas elliptical flows only admit even-n resonances.

Note that the condition (3.32) for resonance readily extends the one by Bayly (1986) for basic elliptical flow instability ($\mathcal{B}=0$ and $\mathcal{N}=0$), so that, $4\Omega\mu=n\Omega_0$, that immediately yielded $\mu=n/4=0.5$ for the elliptical flow ($n=2$) and $n/4=0.25$ for the precessing flow ($n=1$) (see, Kerswell 1993; Salhi & Cambon 2009) giving the origin of time-dependent instability tongues at vanishing ε. We also note that the analysis of triad instability principle by Waleffe (1992) shows that the elliptical instability corresponds to a forward-interaction: the two modes with eigenfrequency $\omega_1=\omega_r$ and $\omega_2=-\omega_r$ have opposite polarities and are coupled with the mean flow, which is associated with a zero frequency, the unstable modes are thereby two resonant inertial waves associated with the uniform background rotation.

4. Asymptotic analysis of the Floquet system

Following the study of the MGE instability by SC23, we extend the asymptotic method of LZ04 to determine, at leading order in ε, the maximal growth rate of the solution of the four-component Floquet system (3.25). We note that the analytical developments presented in the present study are somewhat more complex than those performed by SC23

https://doi.org/10.1017/jfm.2025.10881 Published online by Cambridge University Press

for the elliptic instability. This is mainly due to the fact that the unperturbed basic state for the precessional flow (see (2.18) and (2.19)) is somewhat more complex than that for the elliptic flow.

We indicate that in the remainder of this article the frequencies ω_1, ω_2, ω_3 and ω_4 are normalized by Ω_0, except where they appear in the figures and in (5.3).

4.1. *Expansion in Taylor series of the Floquet multiplier matrix*

We denote by $\boldsymbol{\Phi}(\tau, \varepsilon, \mu, \mathcal{B}, \mathcal{N})$ the fundamental matrix solution,

$$d_\tau \boldsymbol{\Phi} = \boldsymbol{D}\cdot\boldsymbol{\Phi}, \quad \boldsymbol{\Phi}(\tau = 0) = \boldsymbol{I}_4 \tag{4.1}$$

and by $\boldsymbol{M} = \boldsymbol{\Phi}(2\pi, \varepsilon, \mu, \mathcal{B}, \mathcal{N})$ the Floquet multiplier matrix. According to Floquet–Lyapunov theorem, $\boldsymbol{\Phi}$ is expressible in the form (see, Kuchment 1993),

$$\boldsymbol{\Phi}(\tau) = \boldsymbol{F}(\tau)\exp(\boldsymbol{K}\tau), \tag{4.2}$$

where $\boldsymbol{F}(\tau)$ is a non-singular continuous 2π-periodic 4×4 matrix-function (whose derivative is an integrable piecewise-continuous function) and $\boldsymbol{K}$ is a constant matrix. The determinant of $\boldsymbol{\Phi}$ is unity at $\tau = 2\pi$, $|\boldsymbol{\Phi}(2\pi)| = 1$ since

$$\text{trace } \boldsymbol{D} = \sum_{j=1}^{4} D_{jj} = -4\varepsilon\frac{k_2 k_3}{k^2} = -\frac{1}{k^2}d_\tau k^2. \tag{4.3}$$

It follows that whenever λ is an eigenvalue of the monodromy matrix, $\boldsymbol{M} = \boldsymbol{\Phi}(2\pi)$, so also are its inverse λ^{-1} and its complex conjugate $\overline{\lambda}$ (see LZ04). Consequently, in the stable case, eigenvalues of $\boldsymbol{M}$ lie on the unit circle. If any eigenvalue λ of $\boldsymbol{M}$ has modulus exceeding one, this implies that there is indeed an exponentially growing solution. The growth rates are then given by

$$\sigma = \frac{1}{2\pi}\log(\lambda). \tag{4.4}$$

It follows that whenever λ is an eigenvalue of $\boldsymbol{M}$, so also are its inverse λ^{-1} and its complex conjugate $\overline{\lambda}$. We denote by

$$p(\lambda, \varepsilon) = |\boldsymbol{M} - \lambda\boldsymbol{I}_4| \tag{4.5}$$

the characteristic polynomial of the Floquet multiplier matrix $\boldsymbol{M}$ and by Λ_1, Λ_2, Λ_3 and Λ_4 its roots. A necessary condition for stability is that each root lie on the unit circle (see LZ04).

We expand the Floquet multiplier matrix $\boldsymbol{M}(\varepsilon, \mu, \mathcal{B}, \mathcal{N})$ in Taylor series in the neighbourhood of $(\varepsilon, \mu) = (0, \mu_0)$, holding $(\mathcal{B}, \mathcal{N})$ constant,

$$\boldsymbol{M} = \boldsymbol{M}_0(\mu_0, 0) + \varepsilon\boldsymbol{M}_\varepsilon(\mu_0, 0) + (\mu - \mu_0)\boldsymbol{M}_\mu(\mu_0, 0) + \cdots \tag{4.6}$$

where $\boldsymbol{M}_\varepsilon = (\partial\boldsymbol{M}/\partial\varepsilon)$, $\boldsymbol{M}_\mu = (\partial\boldsymbol{M}/\partial\mu)$ and the dots indicate higher-order terms in ε and $\mu - \mu_0$. Generally, at sufficiently small ε, the region in the (ε, μ)-plane where instability occurs is typically a wedge with apex at a point $(\varepsilon, \mu)) = (0, \mu_0)$ and boundaries

$$\mu = \mu_0 + \eta_\pm\varepsilon, \tag{4.7}$$

where the slopes η_+ and η_- are to be found. The instability (if it exists) has a bandwidth $(\eta_+ - \eta_-)\varepsilon$ that is, for given ε, $\mathcal{B}$ and $\mathcal{N}$, the length of the μ-interval for which the wavenumbers are unstable. Therefore, (4.6) can be rewritten as

$$\boldsymbol{M} = \boldsymbol{M}_0 + \varepsilon\boldsymbol{M}_1 + O(\varepsilon^2), \tag{4.8a}$$

$$\boldsymbol{M}_1 = \boldsymbol{M}_\varepsilon + \eta\boldsymbol{M}\mu. \tag{4.8b}$$

https://doi.org/10.1017/jfm.2025.10881 Published online by Cambridge University Press

Accordingly, we no longer need the designation μ_0 and, hereinafter, use the symbol μ in its place.

To determine matrices $\boldsymbol{M}_0$, $\boldsymbol{M}_\varepsilon$ and $\boldsymbol{M}_\mu$, we expand, for a given $\tau \in [0, 2\pi]$, $\boldsymbol{\Phi}$ and $\boldsymbol{D}$,

$$\boldsymbol{\Phi}(\tau, \varepsilon) = \boldsymbol{\Phi}_0(\tau, \mu, 0) + \varepsilon \boldsymbol{\Phi}_1(\tau, \mu, 0) + O(\varepsilon^2), \tag{4.9a}$$

$$\boldsymbol{D}(\tau, \varepsilon) = \boldsymbol{D}_0 + \varepsilon \boldsymbol{D}_\varepsilon(\tau, 0) + O(\varepsilon^2), \tag{4.9b}$$

where $\boldsymbol{\Phi}_0(\tau = 0) = \boldsymbol{I}_4$ and $\boldsymbol{\Phi}_1(\tau = 0) = \boldsymbol{0}$. We notice that we find the same expression for the matrix $\boldsymbol{D}_\varepsilon(\tau, \varepsilon)$ for both KBF and MBF cases (see Appendix B2). Thus, to leading order in ε, the stability problem for these two basic flows is the same.

Substituting (4.9) into (4.1), we obtain

$$d_\tau \boldsymbol{\Phi}_0 = \boldsymbol{D}_0 \cdot \boldsymbol{\Phi}_0, \quad d_\tau \boldsymbol{\Phi}_1 = \boldsymbol{D}_0 \cdot \boldsymbol{\Phi}_1 + \boldsymbol{D}_\varepsilon \cdot \boldsymbol{\Phi}_0, \tag{4.10}$$

with solution $\boldsymbol{\Phi}_0(\tau) = \mathrm{e}^{\tau \boldsymbol{D}_0}$ and

$$\boldsymbol{\Phi}_1(\tau) = \boldsymbol{\Phi}_0(\tau) \cdot \left(\int_0^\tau \boldsymbol{\Phi}_0^{-1}(s) \cdot \boldsymbol{D}_\varepsilon(s) \cdot \boldsymbol{\Phi}_0(s) \mathrm{d}s \right). \tag{4.11}$$

Because the characteristic polynomial $\mathrm{p}(\lambda, \varepsilon)$ is the same in any coordinate system and the four eigenvalues of the matrix $\boldsymbol{D}_0$, given by (3.30) are distinct as long as $\mathcal{B} \neq 0$ and $0 < \mu^2 < 1$, we transform the solution in the basis diagonalizing $\boldsymbol{D}_0$, so that

$$\tilde{\boldsymbol{M}}_0 = \boldsymbol{T}^{-1} \cdot \boldsymbol{M}_0 \cdot \boldsymbol{T} = \mathbf{diag}\left(\mathrm{e}^{2\pi\sigma_1}, \mathrm{e}^{-2\pi\sigma_1}, \mathrm{e}^{2\pi\sigma_3}, \mathrm{e}^{-2\pi\sigma_3}\right) = \mathbf{diag}\,(\lambda_1, \lambda_2, \lambda_3, \lambda_4), \tag{4.12a}$$

$$\tilde{\boldsymbol{M}}_\varepsilon = \boldsymbol{T}^{-1} \cdot \boldsymbol{M}_\varepsilon \cdot \boldsymbol{T} = \tilde{\boldsymbol{M}}_0 \cdot \tilde{\boldsymbol{J}}, \tag{4.12b}$$

$$\tilde{J}_{ij} = \left(\boldsymbol{T}^{-1}\right)_{im} T_{lj} \int_0^{2\pi} \mathrm{e}^{(\sigma_j - \sigma_i)\tau} \left(\boldsymbol{D}_\varepsilon\right)_{ml}(\tau) \mathrm{d}\tau, \tag{4.12c}$$

where the columns of the matrix $\boldsymbol{T}$ are the eigenvectors associated with the eigenvalues σ_j $(j = 1, 2, 3, 4)$ given by (B1) and $\boldsymbol{T}^{-1}$ is its inverse given by (B2).

To complete the construction of the matrix $\tilde{\boldsymbol{M}}_1$, which appears in (4.8), we need the derivative of $\tilde{\boldsymbol{M}}_0(\mu) = \tilde{\boldsymbol{M}}(\mu, 0)$ with respect to μ,

$$\eta \tilde{\boldsymbol{M}}_\mu = \eta \frac{\partial \tilde{\boldsymbol{M}}_0}{\partial \mu} = \frac{2\mathrm{i}\pi\eta}{\Omega} \mathbf{diag}\left(\frac{\partial \omega_1}{\partial \mu}\lambda_1, \frac{\partial \omega_2}{\partial \mu}\lambda_2, \frac{\partial \omega_3}{\partial \mu}\lambda_3, \frac{\partial \omega_4}{\partial \mu}\lambda_4 \right), \tag{4.13}$$

where ω_1, ω_2, ω_3 and ω_4 are given by (3.31).

When there is a subharmonic instability associated with the resonant case $\omega_\ell - \omega_j = \pm 1$ $(j \neq \ell)$, its maximum growth rate σ_m is given by

$$\sigma_m = \frac{\varepsilon}{2\pi} \Re \sqrt{\tilde{J}_{\ell j} \tilde{J}_{j\ell}} \quad (\text{with } \ell \neq j), \tag{4.14}$$

recalling that the frequencies ω_j $(j = 1, 2, 3, 4)$ are normalized by Ω_0. In the following sections, we present the analytical results of the maximum growth rates associated with the three unstable cases, namely the fast–fast, slow–slow and fast–slow destabilizing resonances (calculation details are given in the Supplementary material).

https://doi.org/10.1017/jfm.2025.10881 Published online by Cambridge University Press

4.2. *Case of unstable resonance between two fast modes or between two slow modes*

4.2.1. *Domains of the resonant cases in the* $(\mathcal{B}, \mathcal{N})$*-plane*

The resonance condition between two fast modes is obtained by substituting the expression of ω_1 given by (3.31) into the following identity:

$$\omega_1 - \omega_2 = 2\omega_1 = 1 \Longrightarrow\ 16\omega_1^4 = 1, \tag{4.15}$$

or equivalently,

$$4\mathcal{B}^2\big(\mathcal{B}^2 - \mathcal{N}^2\big)\mu^4 + \big(4\mathcal{B}^2\mathcal{N}^2 - 2\mathcal{B}^2 - 4 + \mathcal{N}^2\big)\mu^2 + \left(\frac{1}{4} - \mathcal{N}^2\right) = 0, \tag{4.16}$$

with $0 < \mu^2 < 1$. Because the replacement $\mu \to -\mu$ in (4.16) result in the same condition, we may therefore assume without loss of generality that $\mu > 0$. We note that the resonant condition between two slow modes, $\omega_3 - \omega_4 = 1$, is also described by (4.16), and the real roots of (4.16), such that $0 < \mu^2 < 1$, if they exist, are ordered. The smaller of the two roots characterizes the resonant cases between two fast modes where

$$(\mathcal{B}, \mathcal{N}) \in [0, +\infty) \times \big[0,\, 1/2\big] \cup \mathcal{D}_f, \quad \lim_{\substack{\mathcal{B}\to+\infty \\ 0\leqslant\mathcal{N}\leqslant\frac{1}{2}}} \mathcal{B}^2\mu^2 = \frac{1}{4} - \mathcal{N}^2, \quad \lim_{\substack{\mathcal{N}\to+\infty \\ \frac{1}{2}<\mathcal{B}\leqslant\frac{\sqrt{5}}{2}}} \mu^2 = \frac{1}{4\mathcal{B}^2}. \tag{4.17}$$

The other root of (4.16), such that $0 < \mu^2 < 1$, characterizes the resonant cases between two slow modes where

$$(\mathcal{B}, \mathcal{N}) \in \big[\sqrt{5}/2, +\infty\big) \times [0, +\infty) \cup \mathcal{D}_f, \quad \lim_{\substack{\mathcal{B}\to+\infty \\ 0\leqslant\mathcal{N}<+\infty}} \mathcal{B}^2\mu^2 = \frac{1}{4}, \quad \lim_{\substack{\mathcal{N}\to+\infty \\ \frac{1}{2}<\mathcal{B}<+\infty}} \mu^2 = 1. \tag{4.18}$$

Here, the domain $\mathcal{D}_f$ is defined as follows (see also figure 2):

$$\forall\,(\mathcal{B}, \mathcal{N}) \in \mathcal{D}_f \Leftrightarrow \text{ for given } \mathcal{N} \in \big(\sqrt{6}/2, +\infty\big) \quad \Longrightarrow \quad \frac{1}{2} < f(\mathcal{N}) \leqslant \mathcal{B} < \frac{\sqrt{5}}{2}, \tag{4.19}$$

where $f : (\sqrt{6}/2, +\infty) \to (1/2, \sqrt{5}/2)$ is a continuous decreasing function

$$\forall \mathcal{N} \in \big(\sqrt{6}/2, +\infty\big),\ f(\mathcal{N}) = \frac{1}{2\mathcal{N}^2}\sqrt{\big(\mathcal{N}^2+2\big)^2 - 6 + 2\sqrt{(4\mathcal{N}^2-1)(\mathcal{N}^4-1)}} \underset{\mathcal{N}\to+\infty}{\longrightarrow} \frac{1}{2}. \tag{4.20}$$

For the pure hydrodynamic case ($\mathcal{B} = 0, \mathcal{N} = 0$), one has $\mu = 1/4$. For the resonant cases between to fast modes and for given $\mathcal{N} \in [0, 1/2]$, the parameter μ decreases from $\mu = (\sqrt{1-4\mathcal{N}^2})/(2\sqrt{4-\mathcal{N}^2})$ as $\mathcal{B}$ increases, approaching zero when $\mathcal{B} \to +\infty$. Likewise, for given $1/2 < \mathcal{B} = \mathcal{B}_f \leqslant \sqrt{5}/2$ such that $(\mathcal{N}, \mathcal{B}) \in \mathcal{D}_f$, μ increases from $\mu(f^{-1}(\mathcal{B}_f), \mathcal{B}_f)$ approaching 1 when $\mathcal{N} \to +\infty$ (see also figure 3*a*).

For the resonant cases between two slow modes, which exist only in the magnetized case, and for given $\mathcal{B} \in [\sqrt{5}/2, +\infty)$, μ decreases from $\mu = 1/(2(\sqrt{1+\mathcal{B}^2}-1))$ as $\mathcal{N}$ increases approaching $1/(2\mathcal{B})$ when $\mathcal{N} \to +\infty$. Likewise, for given $1/2 < \mathcal{B} \leqslant \sqrt{5}/2$, so that $(\mathcal{N}, \mathcal{B}) \in \mathcal{D}_f$, μ decreases from $\mu(f^{-1}(\mathcal{B}), \mathcal{B})$ approaching $1/(2\mathcal{B})$ when $\mathcal{N} \to +\infty$ (see also figure 3*a*).

https://doi.org/10.1017/jfm.2025.10881 Published online by Cambridge University Press

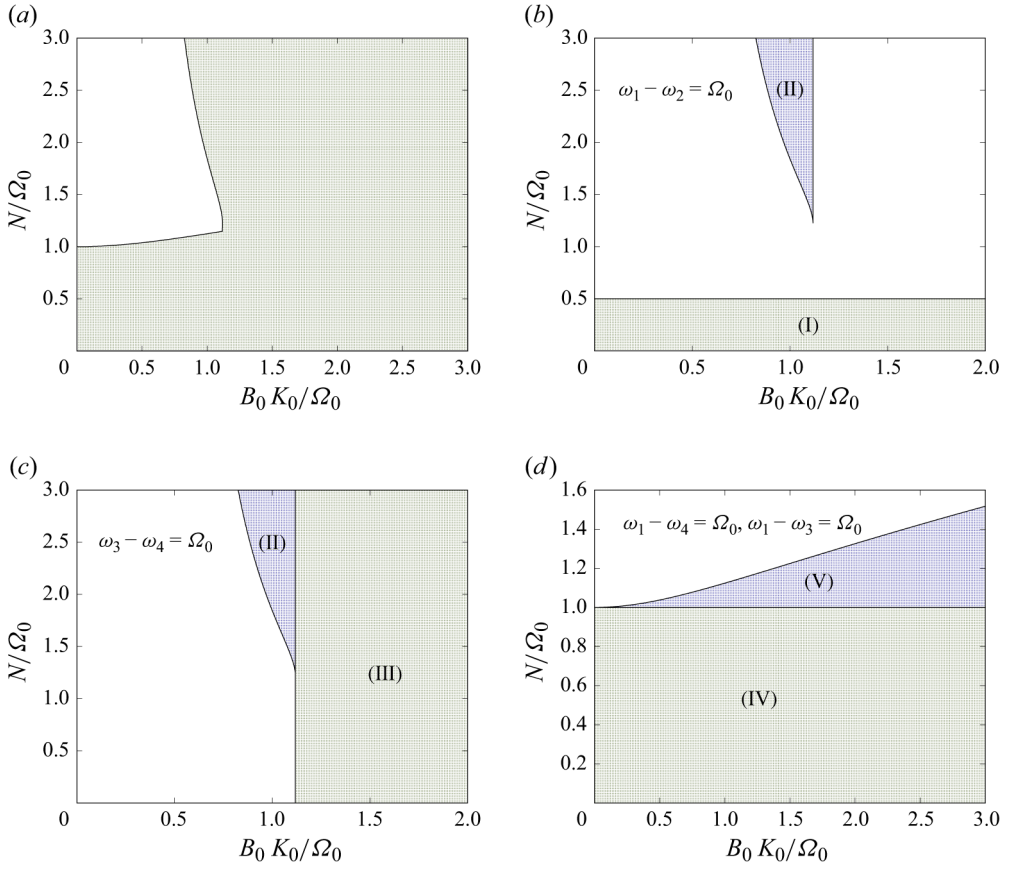


Figure 2. Resonant cases of MIG waves. (*a*) Resonant cases (of order $n = 1$) occur for $(\mathcal{B}, \mathcal{N})$ belonging to the coloured domains. (*b*) Resonance between two fast modes ($\omega_1 - \omega_2 = \Omega_0$) where (I) $\equiv [0, +\infty) \times [0, 1]$ and (II) $\equiv \mathcal{D}_f$ (see (4.19)). (*c*) Resonance between two slow modes ($\omega_3 - \omega_4 = \Omega_0$) where (III) $\equiv [\sqrt{5}/2, +\infty) \times [0, +\infty)$. (*d*) Resonance between a fast mode and a slow mode ($\omega_1 - \omega_4 = \Omega_0$ or $\omega_1 - \omega_3 = \Omega_0$) where (IV) $\equiv [0, +\infty) \times [0, 1]$ and (V) $\equiv \mathcal{D}_m$ (see (4.30)).

4.2.2. *Maximal growth rate*

If a subharmonic instability resulting from the resonance between two fast (respectively, slow) modes exists, its maximal growth rate, denoted by σ_{mf} (σ_{ms}), is given by

$$\sigma_{mf} = \frac{\varepsilon}{2\pi} \Re \sqrt{\tilde{J}_{12} \tilde{J}_{21}}, \quad \sigma_{ms} = \frac{\varepsilon}{2\pi} \Re \sqrt{\tilde{J}_{34} \tilde{J}_{43}}. \tag{4.21}$$

After some analytical developments given in the Supplementary material, we find

$$\frac{\sigma_{mf}}{\varepsilon}, \frac{\sigma_{ms}}{\varepsilon} = \left| \frac{\left(4\mathcal{B}^2\mu^2 + 1\right) \mu \sqrt{1 - \mu^2}}{8\left[2\left(4 + 2\mathcal{B}^2 - \mathcal{N}^2\right)\mu^2 + 2\mathcal{N}^2 - 1\right]} \right| \times \left| \left(\left(4\mathcal{B}^2\mu^2 - 1\right)\left(\mathcal{B}^2\left(1 - 4\mathcal{N}^2 - 4\left(\mathcal{B}^2 - \mathcal{N}^2\right)\mu^2\right) + 4\right) + 2\left(4\mathcal{B}^2\mu^2 - 3\right)\right) \right|, \tag{4.22}$$

in which $0 < \mu^2 < 1$ is the smaller of the two roots of (4.16) when it is a resonance between two fast modes or the other root when it is a resonance between two slow modes.

https://doi.org/10.1017/jfm.2025.10881 Published online by Cambridge University Press

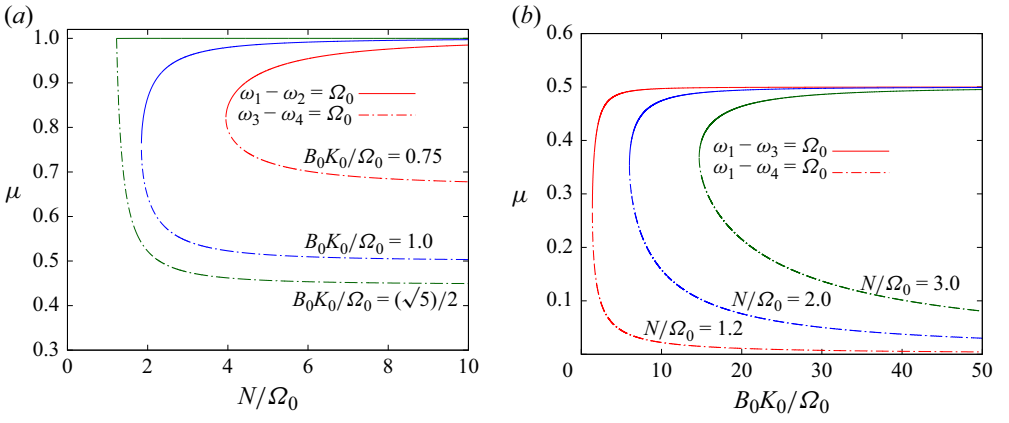


Figure 3. Resonant cases of MIG waves. (*a*) Variation of the parameter $\mu = k_0/K_0$ versus $\mathcal{N} = N/\Omega_0$ for $\mathcal{B} = B_0K_0/\Omega_0 = 0.75,\ 1.0,\ \sqrt{5}/2$ such that $(\mathcal{B}, \mathcal{N}) \in \mathcal{D}_f$ (see (4.19)) associated with the resonant cases between two fast modes ($\omega_1 - \omega_2 = \Omega_0$) or between two slow modes ($\omega_3 - \omega_4 = \Omega_0$). (*b*) Variation of the parameter $\mu = k_0/K_0$ versus $\mathcal{B}$ for $\mathcal{N} = 1.2,\ 2.0,\ 3.0$ such that $(\mathcal{B}, \mathcal{N}) \in \mathcal{D}_m$ (see (4.30)) associated with the resonant cases between a fast mode and a slow mode ($\omega_1 - \omega_4 = \Omega_0$ or $\omega_1 - \omega_3 = \Omega_0$). Here, $K_0 = \sqrt{k_0^2 + k_p^2}$.

Some results reported in previous studies of stratified or magnetized precessing flows can be recovered from (4.22),

$$\text{for } \mathcal{B} = \mathcal{N} = 0, \quad \mu = \frac{1}{4}, \quad \frac{\sigma_{mf}}{\varepsilon} = \frac{5\sqrt{15}}{32}, \tag{4.23a}$$

$$\text{for } \mathcal{B} = 0, \quad \mu = \frac{1}{2}\sqrt{\frac{1-4\mathcal{N}^2}{4-\mathcal{N}^2}}, \quad \frac{\sigma_{mf}}{\varepsilon} = \frac{5\sqrt{15}}{8}\frac{\sqrt{1-4\mathcal{N}^2}}{\left(4-\mathcal{N}^2\right)}, \tag{4.23b}$$

$$\text{for } \mathcal{N} = 0, \ \mu = \frac{1}{2\left(\sqrt{1+\mathcal{B}^2}+1\right)}, \ \frac{\sigma_{mf}}{\varepsilon} = \frac{1}{8}\frac{\left(2\sqrt{\mathcal{B}^2+1}+3\right)\sqrt{4\left(1+\sqrt{1+\mathcal{B}^2}\right)^2-1}}{\left(1+\sqrt{\mathcal{B}^2+1}\right)^2}. \tag{4.23c}$$

Equation (4.23*b*) indicates that the maximal growth rate is zero at $\mathcal{N} = 1/2$. Therefore, in the non-magnetized stratified precessing case ($\mathcal{B} = 0$), the subharmonic instability is completely suppressed by stratification when $\mathcal{N}$ reaches $1/2$ (see, Benkacem *et al.* 2022). For the non-stratified magnetized precessing case ($\mathcal{N} = 0$), (4.23*c*) indicates that σ_{mf}/ε decreases as $\mathcal{B}$ increases so as

$$\lim_{\mathcal{N}=0,\ \mathcal{B}\to+\infty} \frac{\sigma_{mf}}{\varepsilon} = \frac{1}{2}. \tag{4.24}$$

Recall that, at small scales, i.e. $\sqrt{k_p^2 + k_0^2} \gg 1$, $\mathcal{B}$ is large even if $B_0/\Omega_0 \sim 1$.

In the stratified magnetized precessing case, the analysis of (4.22) is more subtle as shown in the following.

For $0 < \mathcal{N} < 0.5$, we verify using the second identity in (4.17) that σ_{mf} approaches zero for large $\mathcal{B}$. Given (4.24), this clearly proves that the $\mathcal{N} \to 0$ limit is, in fact, singular (discontinuous).

For $\mathcal{N} = 0.5$, (4.16) gives $\mu = 0$ (i.e. the smaller of the two roots) and hence, $\sigma_{mf} = 0$, signifying that there is no parametric instability associated with the resonant case of order

https://doi.org/10.1017/jfm.2025.10881 Published online by Cambridge University Press

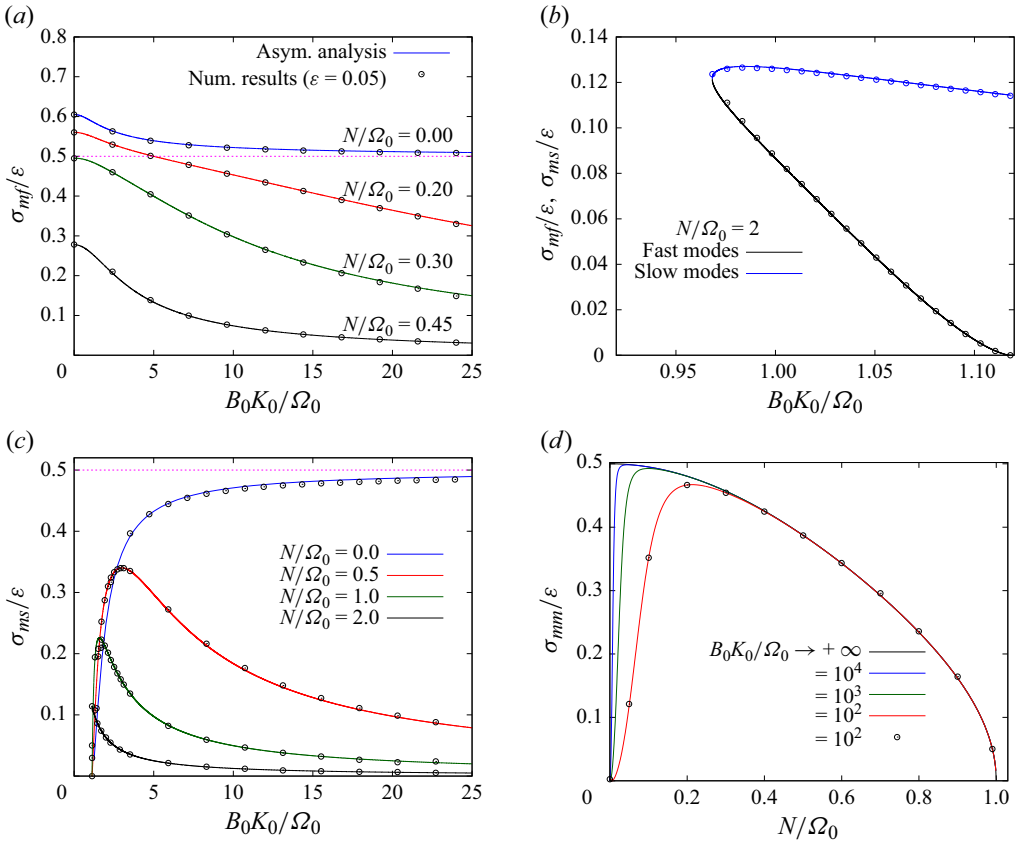


Figure 4. Maximal growth rate of destabilizing resonant cases given by the asymptotic formulae. (*a*) Resonant cases between two fast modes for some values of $(\mathcal{B}, \mathcal{N}) \in [0, +\infty) \times [0, 1/2]$. (*b*) Resonant cases between two fast modes or between two slow modes for some values of $(\mathcal{B}, \mathcal{N}) \in \mathcal{D}_f$ (see (4.19)). (*c*) Resonant cases between two slow modes for some values of $(\mathcal{B}, \mathcal{N}) \in [\sqrt{5}/2, +\infty) \times [0, +\infty)$. (*d*) Resonant cases between a fast mode and a slow mode for some values of $(\mathcal{B}, \mathcal{N}) \in [0, +\infty) \times [0, 1]$. The numerical results obtained for $\varepsilon = 0.05$ (symbol) are also reported.

$n = 1$ between two fast modes. It is worth mentioning that the case $\mu = 0$, so that $k_0 = 0$ corresponds to a 2-D three component (2D3C) flow (see the end of § 3.3.2).

For $1/2 < \mathcal{B} \leqslant \sqrt{5}/2$, i.e. $(\mathcal{B}, \mathcal{N}) \in \mathcal{D}_f$, we verify using the third identity in (4.17) that σ_{mf} also approaches zero for large $\mathcal{N}$.

Figure 4(*a*) shows σ_{mf}/ε versus $\mathcal{B}$ for $\mathcal{N} = 0,\ 0.2,\ 0.3,\ 0.35$ and $\mathcal{N} = 0.45$, so that $(\mathcal{B}, \mathcal{N}) \in [0, +\infty) \times [0, 1/2]$, while figure 4(*b*) illustrates the variation of σ_{mf}/ε versus $\mathcal{B}$ for $\mathcal{N} = 2$, so that $(\mathcal{B}, \mathcal{N}) \in \mathcal{D}_f$. The numerical results for $\varepsilon = 0.05$, which will be discussed in § 5, are also reported .

For the non-stratified magnetized case ($\mathcal{N} = 0$), the expression of the maximal growth rate σ_{ms} of the destabilizing resonance between two slow mode deduced from (4.22) is of the form

$$\frac{\sigma_{ms}}{\varepsilon} = \frac{\left(2 + 2\mathcal{B}^2 - 3\sqrt{\mathcal{B}^2 + 1}\right)\sqrt{4\left(\sqrt{1 + \mathcal{B}^2} - 1\right)^2 - 1}}{8\sqrt{1 + \mathcal{B}^2}\left(\sqrt{\mathcal{B}^2 + 1} - 1\right)^2} \underset{\mathcal{B}\to+\infty}{\longrightarrow} \frac{1}{2} \tag{4.25}$$

https://doi.org/10.1017/jfm.2025.10881 Published online by Cambridge University Press

where $\sqrt{5}/2 < \mathcal{B} < +\infty$, in agreement with the previous results by Salhi *et al.* (2010). In this case, σ_{ms}/ε increases from 0 at $\mathcal{B} = \sqrt{5}/2$ to 1/2 as $\mathcal{B} \to +\infty$.

For the stratified magnetized case such that $(\mathcal{B}, \mathcal{N}) \in [\sqrt{5}/2, +\infty) \times [0, +\infty) \cup \mathcal{D}_f$, we use the second and third identities in (4.18) to deduce from (4.22) that

$$\lim_{\mathcal{N}>0,\ \mathcal{B}\to+\infty} \frac{\sigma_{ms}}{\varepsilon} = 0, \qquad \lim_{\mathcal{B}>\frac{1}{2},\ \mathcal{N}\to+\infty} \frac{\sigma_{ms}}{\varepsilon} = 0. \tag{4.26}$$

Figure 4(*c*) shows σ_{ms}/ε versus $\mathcal{B}$ for $\mathcal{N} = 0,\ 0.5,\ 1$ and $\mathcal{N} = 2$, so that $(\mathcal{B}, \mathcal{N}) \in [0, +\infty) \times [\sqrt{5}/2, +\infty)$, while figure 4(*b*) illustrates the variation of σ_{ms}/ε versus $\mathcal{B}$ for $\mathcal{N} = 2$, so that $(\mathcal{B}, \mathcal{N}) \in \mathcal{D}_f$. These figures show the expected agreement between the numerical results and the asymptotic formulae.

Accordingly, we may conclude that, unlike the non-stratified magnetized case for which $\lim_{\mathcal{B}\to+\infty} \sigma_{ms}/\varepsilon = 1/2$, the destabilizing resonance between two slow modes is weakened in the presence of stable stratification in the sense that its growth rate is reduced and approaches zero for strong stratification. Given (4.25), this clearly proves that the $\mathcal{N} \to 0$ limit is, in fact, singular (discontinuous).

4.3. *Destabilizing resonance between a slow mode and a fast mode*

In this section, we will show that the resonant case associated with $\omega_1 - \omega_4 = 1$ is destabilizing. In contrast, the resonant case associated with $\omega_1 - \omega_3 = 1$ is stable.

By substituting the expression of ω_1^2 and ω_3^2 given by (3.31) into the following identity:

$$\omega_1 - \omega_4 = \omega_1 + \omega_3 = 1 \Longrightarrow \omega_1^4 + \omega_3^4 - 2\omega_1^2\omega_3^2 - 2\big(\omega_1^2 + \omega_3^2\big) + 1 = 0, \tag{4.27}$$

we obtain

$$\Big(\big(4 - \mathcal{N}^2\big)^2 + 16\mathcal{B}^2\Big)\mu^4 - 2\Big(2\mathcal{B}^2 + \big(\mathcal{N}^2 - 4\big)\big(\mathcal{N}^2 - 1\big)\Big)\mu^2 + \big(\mathcal{N}^2 - 1\big)^2 = 0. \tag{4.28}$$

We note that the resonant condition $\omega_1 - \omega_3 = 1$, is also described by (4.16), and the real roots of (4.16), such that $0 < \mu^2 < 1$, if they exist, are ordered. The smaller of the two roots characterizes the resonant cases characterized by $\omega_1 - \omega_4 = 1$ where

$$(\mathcal{B}, \mathcal{N}) \in (0, +\infty) \times [0, 1] \cup \mathcal{D}_m, \qquad \lim_{\mathcal{B}\to+\infty \mathcal{N}\in[0,+\infty[} \mathcal{B}^2\mu^2 = \frac{\big(1 - \mathcal{N}^2\big)^2}{4}. \tag{4.29}$$

Here, the domain $\mathcal{D}_m$ is defined as follows:

$$\forall\, (\mathcal{B}, \mathcal{N}) \in \mathcal{D}_m \Leftrightarrow \text{ for given } \mathcal{N} \in]1, +\infty[\implies 0 < \sqrt{3\mathcal{N}^2\big(\mathcal{N}^2 - 1\big)} \leqslant \mathcal{B}\,. \tag{4.30}$$

Accordingly, for given $\mathcal{N} \in [0, 1[$, $\mu(\mathcal{B}, \mathcal{N})$ decreases from $\mu(0, \mathcal{N}) = \sqrt{(1 - \mathcal{N}^2)/(4 - \mathcal{N}^2)}$ as $\mathcal{B}$ increases approaching zero when $\mathcal{B} \to +\infty$. For $\mathcal{N} = 1$, one has $\mu = 0$, and hence there is no instability for this resonant case (see the end of § 3.3.2). For given $\mathcal{N} > 1$, such that $(\mathcal{B}, \mathcal{N}) \in \mathcal{D}_m$, $\mu(\mathcal{B}, \mathcal{N})$ decreases from $\mu(\mathcal{B}_m, \mathcal{N}) = \sqrt{(\mathcal{N}^2 - 1)/(7\mathcal{N}^2 - 4)}$, approaching zero when $\mathcal{B} \to +\infty$, where $\mathcal{B}_m^2 = 3\mathcal{N}^2(\mathcal{N}^2 - 1)$ (see also figure 2*c*).

The maximal growth rate of the destabilizing resonant case $\omega_1 - \omega_4 = 1$, is denoted by σ_{mm} (m for mixed) is then described by (4.14) which, in this case, reduces to

$$\sigma_{mm} = \frac{\varepsilon}{2\pi}\,(\Re\alpha)_{max} = \frac{\varepsilon}{2\pi}\Re\sqrt{\tilde{J}_{14}\tilde{J}_{41}} \tag{4.31}$$

https://doi.org/10.1017/jfm.2025.10881 Published online by Cambridge University Press

where

$$\frac{\tilde{J}_{14}}{2\mathrm{i}\pi}=\frac{\mu\sqrt{1-\mu^2}}{\left(\omega_3^2-\omega_1^2\right)}\left[\frac{\left(\mu^2\mathcal{B}^2-\omega_3^2\right)\omega_1\omega_3}{\mu^2\mathcal{B}^2}+\frac{\left(\mu^2\mathcal{B}^2-\omega_3^2\right)^2}{4\mu^4\mathcal{B}^2}\frac{\omega_1}{\omega_3}\left(\omega_3-\left(1-\mu^2\right)\mathcal{N}^2\right)\right.$$
$$\left.+\left(4\mu^2-1\right)\omega_3-\mathcal{N}^2\left(1-\mu^2\right)\frac{\left(\mu^2\mathcal{B}^2-\omega_3^2\right)}{\omega_3}\right], \tag{4.32}$$

$$\frac{\tilde{J}_{41}}{2\mathrm{i}\pi}=\frac{\mu\sqrt{1-\mu^2}}{\left(\omega_3^2-\omega_1^2\right)}\left[\frac{\left(\mu^2\mathcal{B}^2-\omega_1^2\right)\omega_1\omega_3}{\mu^2\mathcal{B}^2}+\frac{\left(\mu^2\mathcal{B}^2-\omega_1^2\right)^2}{4\mu^4\mathcal{B}^2}\frac{\omega_3}{\omega_1}\left(\omega_1-\left(1-\mu^2\right)\mathcal{N}^2\right)\right.$$
$$\left.+\left(4\mu^2-1\right)\omega_1-\mathcal{N}^2\left(1-\mu^2\right)\frac{\left(\mu^2\mathcal{B}^2-\omega_1^2\right)}{\omega_1}\right], \tag{4.33}$$

where detail calculations are given in the Supplementary material.

In the non-magnetized case ($\mathcal{N}=0$) the resulting expression of σ_{mm} is given by

$$\frac{\sigma_{mm}}{\varepsilon}=\frac{\mathcal{B}^2\sqrt{3+4\mathcal{B}^2}}{8\left(1+\mathcal{B}^2\right)^2}\underset{\mathcal{B}\to+\infty}{\longrightarrow}0. \tag{4.34}$$

However, in the magnetized case, analytically obtaining a compact form for the product $\tilde{J}_{14}\tilde{J}_{41}$ that only involves the parameters μ, $\mathcal{N}$ and $\mathcal{B}$ is quite complex. Nevertheless, some results characterizing the behaviour of σ_{mm} can be drawn by analysing the behaviour of $\tilde{J}_{14}\tilde{J}_{41}$ for large $\mathcal{B}$. Recall that, at small scales, i.e. $\sqrt{k_p^2+k_0^2}\gg 1$, $\mathcal{B}$ is large even if $B_0/\Omega_0\sim 1$.

Using the second identity in (4.29) we deduce the following equivalent forms for the normalized frequencies ω_1 and ω_3 given by (3.31),

$$\omega_1\underset{\mathcal{B}\to+\infty}{\sim}\frac{1+\mathcal{N}^2}{2},\quad \omega_3\underset{\mathcal{B}\to+\infty}{\sim}\mu\mathcal{B}\underset{\mathcal{B}\to+\infty}{\sim}\frac{1-\mathcal{N}^2}{2}, \tag{4.35}$$

so that $\omega_1+\omega_3=\omega_1-\omega_4=1$. The resulting equivalent form for the product $\tilde{J}_{14}\tilde{J}_{41}$ is given by

$$\frac{\tilde{J}_{14}\tilde{J}_{41}}{4\pi^2}\underset{\mathcal{B}\to+\infty}{\sim}\frac{\omega_3^2}{4\mu^2\mathcal{B}^2}\frac{\left(\mu^2\mathcal{B}^2-\omega_1^2\right)^2}{\left(\omega_3^2-\omega_1^2\right)^2}\left(1-\frac{\mathcal{N}^2}{\omega_1}\right)\underset{\mathcal{B}\to+\infty}{\sim}\frac{1}{4}\frac{\left(1-\mathcal{N}^2\right)}{\left(1+\mathcal{N}^2\right)}. \tag{4.36}$$

Thus, the maximal growth rate of the destabilizing resonance between a fast mode and a slow mode such that $\omega_1-\omega_4=1$ has the following behaviour:

$$\frac{\sigma_{mm}}{\varepsilon}\underset{\mathcal{B}\to+\infty}{\sim}\frac{1}{2}\sqrt{\frac{1-\mathcal{N}^2}{1+\mathcal{N}^2}}. \tag{4.37}$$

Figure 4(d) shows the variation of σ_{mm}/ε versus $\mathcal{N}$ for $\mathcal{B}=10^2,\ 10^3,\ 10^4$ and $\mathcal{B}\to+\infty$. The numerical results obtained for $\varepsilon=0.05$ and $\mathcal{B}=10^2$ are also displayed in figure 4(d). As it can be seen, there is a good agreement between the numerical results (see § 5) and the asymptotic formulae.

Because in the non-magnetized case ($\mathcal{N}=0$), σ_{mm} tends to zero as $\mathcal{B}\to+\infty$ (see 4.34), while in the magnetized case (4.37) gives

$$\lim_{\mathcal{B}\to+\infty\mathcal{N}\to0^+}\frac{\sigma_{mm}}{\varepsilon}=\frac{1}{2}, \tag{4.38}$$

https://doi.org/10.1017/jfm.2025.10881 Published online by Cambridge University Press

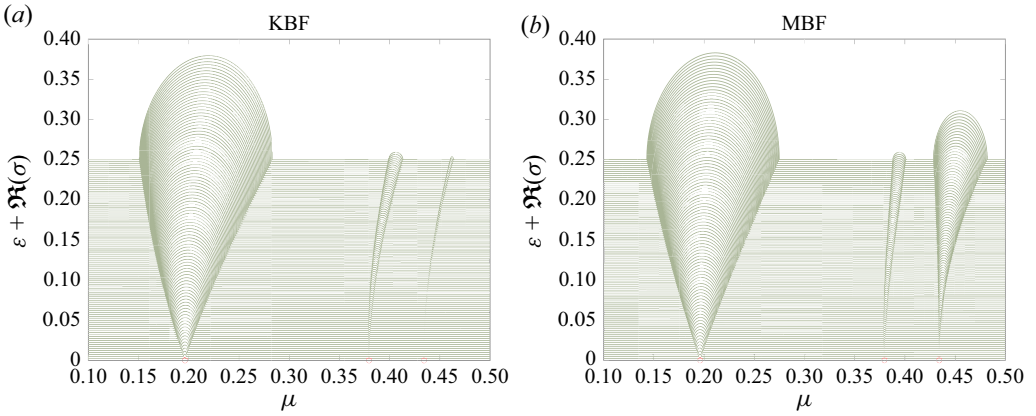


Figure 5. Magneto-gravity-precessional instabilities. The figure shows, for fixed ε, $\varepsilon + \Re\sigma$ versus μ for $\mathcal{B} = 0.75$ and $\mathcal{N} = 0.25$ and 100 values of ε evenly distributed in the interval $[0, 0.25]$. (*a*) The case of KBF; (*b*) the case of MBF. The instability region emanating from the point ($\mu = 0.196$, $\varepsilon + \Re\sigma = 0$) is associated with the destabilizing resonance (of order $n = 1$) between two fast modes, while that emanating from the point ($\mu = 0.380$, $\varepsilon + \Re\sigma = 0$) is associated with the destabilizing resonance (of order $n = 1$) between a fast mode and a slow mode. The third region, which emanates from the point ($\mu = 0.434$, $\varepsilon + \Re\sigma = 0$), characterizes the destabilizing resonance of order $n = 2$ between two fast modes.

we can conclude that for the destabilizing resonance associated with $\omega_1 - \omega_4 = 1$, the limit $\mathcal{N} \to 0$ is also, in fact, singular (discontinuous). This signifies that, at large $\mathcal{B}$, the presence of stable stratification enhances the destabilizing resonance between a fast (hydrodynamic) mode and a slow (magnetic) mode, provided $0 < \mathcal{N} < 1$. This would be relevant for the study of the generation of mean electromotive force ($\mathcal{E} = \langle \boldsymbol{u} \times \boldsymbol{b} \rangle$, (see, Moffatt 1978; Moffatt & Dormy 2019) in strongly magnetized precessing flows under a weak (stable) axial stratification, especially since in the present analysis the electromotive force generation mechanism does not require diffusivity to operate (see, Mizerski, Bajer & Moffatt 2012) for the case of the magneto-elliptic instability of rotating systems).

5. Numerical results

In this section we present a selection of numerical results. These are obtained by integrating the system given by (3.25) to obtain the fundamental matrix solution $\boldsymbol{\Phi}(\tau, \mu, \varepsilon, \mathcal{B}, \mathcal{N})$ (see (4.1)) and evaluating it at $\tau = 2\pi$ to get the Floquet matrix $\boldsymbol{M}(\mu, \varepsilon, \mathcal{B}, \mathcal{N})$.

5.1. *Identification of the instability tongues*

For fixed $(\mathcal{B}, \mathcal{N})$, we use the resonance conditions (4.16), and (4.28) for the identification of instabilities of order $n = 1$ (if they exist). Note that the (3.32) also allows us to identify the high-order destabilizing resonances ($n \geqslant 2$) which are excluded by the procedure leading to the asymptotic formulae. On the other hand, for the same value of the couple $(\mathcal{B}, \mathcal{N})$, we consider several values of ε uniformly distributed in the interval $(0, 0.25)$ and, for each of these values of ε, we integrate numerically the Floquet system (4.1) and determine the growth rate $\Re\sigma$ (corresponding to the maximum modulus eigenvalue) for 5000 values of μ (evenly distributed) in $(0, 1)$. Obviously, $\sigma(\mu) = 0$ if there is no instability. Thus, in the plane $(\mu, \varepsilon + \Re\sigma)$, the region of instability that emanates from the point of abscissa μ characterizes a subharmonic instability as illustrated by figure 5

https://doi.org/10.1017/jfm.2025.10881 Published online by Cambridge University Press

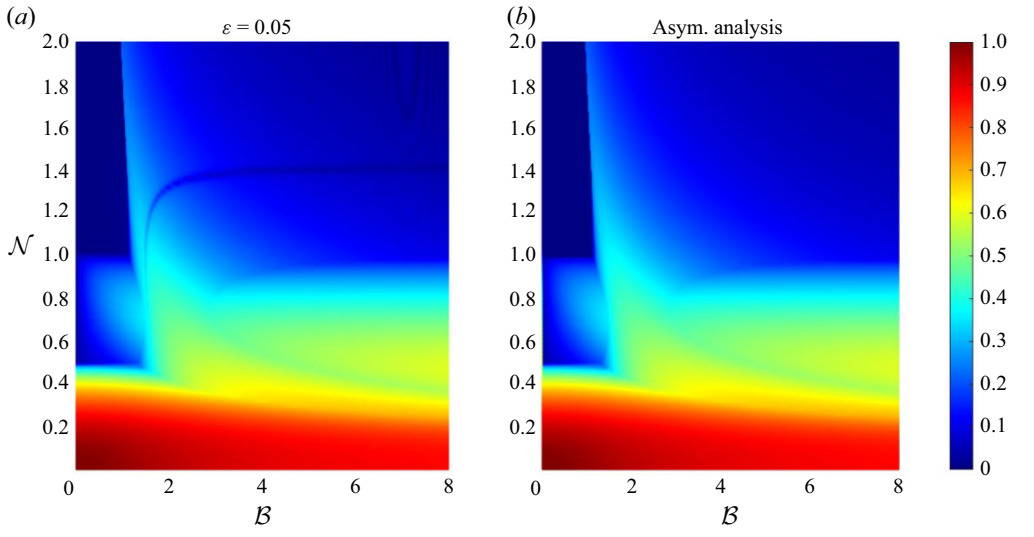


Figure 6. Magneto-gravity-precessional instabilities. Maximal growth rate of dominant instability normalized by $\sigma_0 = (5\sqrt{15}/32)\varepsilon$ plotted as a function of $0 \leqslant \mathcal{B} = K_0 B_0/\Omega_0 \leqslant 8$ and $0 \leqslant \mathcal{N} = N/\Omega_0 \leqslant 2$: (*a*) numerical results for $\varepsilon = 0.05$; (*b*) asymptotic analysis results.

obtained for $\mathcal{B} = 0.75$ and $\mathcal{N} = 0.25$. For these values, the destabilizing resonances detected by the computations are that between two fast modes which correspond to the tongue emanating from the point $(\mu = 0.196, \varepsilon + \Re\sigma = 0)$, and that between a fast mode and a slow mode which corresponds to the tongue emanating from the point $(\mu = 0.380, \varepsilon + \Re\sigma = 0)$. The third instability tongue detected by the calculations emanates from the point $(\mu = 0.434, \varepsilon + \Re\sigma = 0)$ and characterizes the destabilizing resonance of order $n = 2$ between two fast modes. We note that this instability is more developed in the MBF case than in the KBF case, recalling that the matrix $\boldsymbol{D}$ in (3.23) does not have the same expression for these two base flows (see (3.24) and (A13)), except at order $O(\varepsilon)$ (see (B4)).

For both background flows (KBF and MBF), the agreement between the asymptotic formulae and the numerical results is quite good for sufficiently small $\varepsilon(\leqslant 0.05)$, as illustrated in figures 4, 6 and 7. On the other hand, when ε is not small enough, say $0.05 < \varepsilon < 0.25$, the subharmonic instabilities are strongest only in the KBF case, so the agreement between the asymptotic formulae and the numerical results is also quite good (see figures 7*a* and 8*a*).

In figures 6 and 7, we show the continuous variation of the maximal growth rate σ_m (maximum σ over $0 \leqslant \mu \leqslant 1$) of the dominant instability, normalized by $\sigma_0 = (5\sqrt{15}/32)\varepsilon$, plotted as a function of $0 \leqslant \mathcal{B} \leqslant 8$ and $0 \leqslant \mathcal{N} \leqslant 2$. Figure 6(*a*) displays the numerical results obtained for $\varepsilon = 0.05$ in the KBF case, while figure 6(*b*) shows the analytical results σ_m/σ_0 where

$$\sigma_m = \max(\sigma_{mf}, \sigma_{ms}, \sigma_{mm}), \tag{5.1}$$

recalling that σ_{mf}, σ_{ms} and σ_{mm} are given by (4.22) and (4.31), respectively. The numerical results for $\varepsilon = 0.2$ are shown in figure 7 (figure 7*a*, KBF case; figure 7*b*, MBF case). Figure 8 shows σ_m/ε as a function of $\mathcal{N}$ for $\mathcal{B} = 5$, $\varepsilon = 0.05$, 0.1 and $\varepsilon = 0.2$. The analytical results are also reported in figure 8.

https://doi.org/10.1017/jfm.2025.10881 Published online by Cambridge University Press

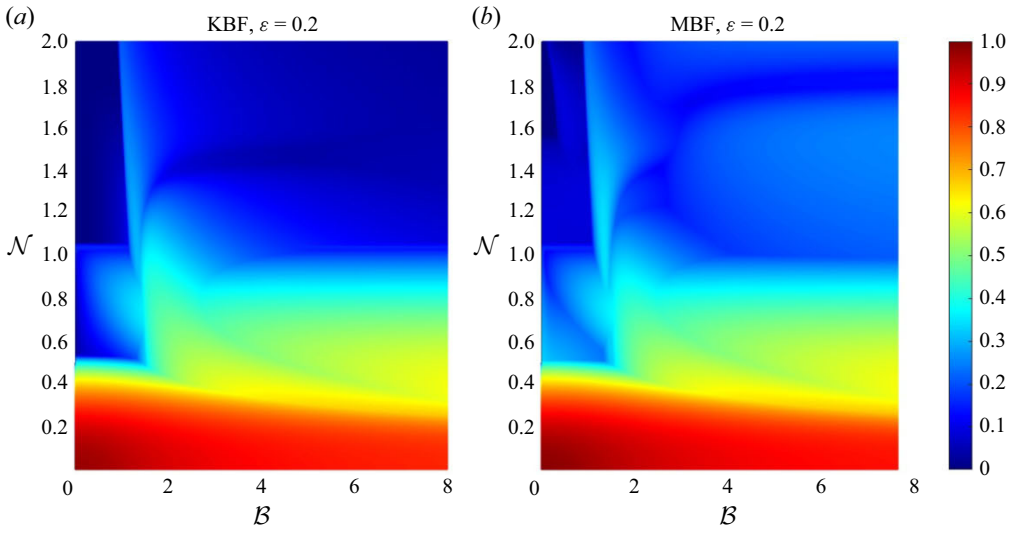


Figure 7. Magneto-gravity-precessional instabilities. Maximal growth rate of dominant instability normalized by $\sigma_0 = (5\sqrt{15}/32)\varepsilon$ plotted as a function of $0 \leqslant \mathcal{B} = K_0 B_0/\Omega_0 \leqslant 8$ and $0 \leqslant \mathcal{N} = N/\Omega_0 \leqslant 2$ for $\varepsilon = 0.2$. Here (*a*) KBF; (*b*) MBF.

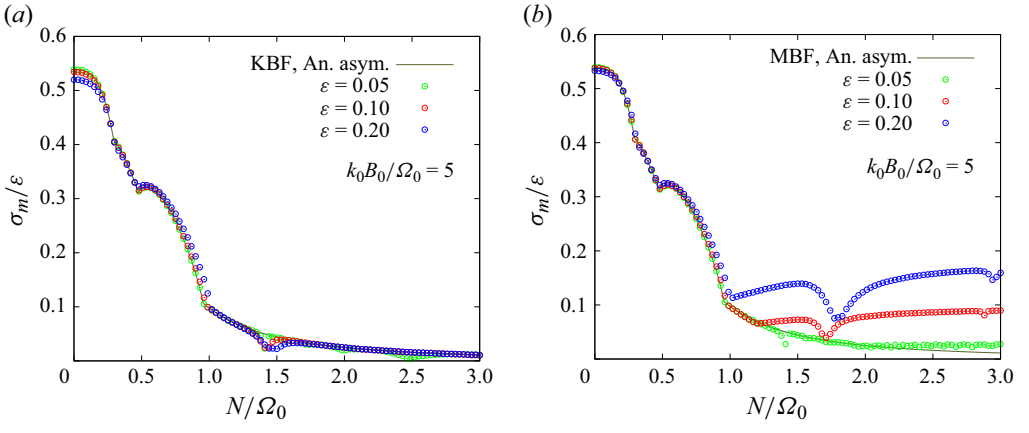


Figure 8. Magneto-gravity-precessional instabilities. Maximal growth rate of dominant instability normalized by $\sigma_0 = (5\sqrt{15}/32)\varepsilon$ plotted as a function of $\mathcal{N} = N/\Omega_0$ for $\mathcal{B} = k_0 B_0/\Omega_0 = 5$ and $\varepsilon = 0.05,\ 0.10,\ 0.20$. Here (*a*) KBF; (*b*) MBF.

In the case of MBF and when ε is not sufficiently small, it is rather the destabilizing resonance of order $n = 2$ between two slow modes which is the strongest provided that $\mathcal{N} > 1$ and $\mathcal{B} > 2$, as illustrated by figures 7(*b*) and 8(*b*). Recall that high-order destabilizing resonances ($n \geqslant 2$) are excluded by the procedure leading to the asymptotic formulae.

5.2. *Diffusive effects in the case where $\nu = \eta = \kappa$*

In this section, we consider the case where $\nu = \eta = \kappa$, so that the magnetic and thermal numbers are equal to one. In this case and given the definition (3.29), we show that the

https://doi.org/10.1017/jfm.2025.10881 Published online by Cambridge University Press

frequency of MIG waves is given by

$$\omega_j^{(v)} = \omega_j + \mathrm{i}\nu k^2 \quad (j = 1, 2, 3, 4), \tag{5.2}$$

where the superscript (v) characterizes the viscous case and ω_j is the frequency of MIG waves for a non-diffusive fluid which is given by (3.30). Therefore, the condition of resonance

$$\omega_j^{(v)} - \omega_\ell^{(v)} = \omega_j - \omega_\ell = n\Omega_0, \quad (\ell \neq j) \tag{5.3}$$

is not modified when $\nu = \eta = \kappa$. As for the destabilizing resonances (if they exist), they are affected by viscosity as shown in the following.

We formally rewrite the system (3.20) as

$$d_\tau \hat{c}_j = \mathcal{L}_{jm}\hat{c}_m \quad (j, m = 1, \cdots, 5). \tag{5.4}$$

By taking into account diffusive terms such that $\nu = \eta = \kappa$, the above system is transformed as

$$d_\tau \hat{c}_j^{(v)} = \mathcal{L}_{jm}\hat{c}_m^{(v)} - \Omega_0^{-1}\nu k^2 \hat{c}_j^{(v)} \quad (j, m = 1, \cdots, 5), \tag{5.5}$$

where its solution can be expressed in terms of that of (5.4) as

$$\hat{c}_j^{(v)}(\tau) = \hat{c}_j(\tau)\exp\left(-\frac{\nu}{\Omega_0}\int_0^\tau k^2(s)\mathrm{d}s\right). \tag{5.6}$$

Thus, the linear part of the spectral counterpart of MIPS is zero because, for purposes of studying stability, we have set $\hat{\varpi}_m = 0$ (see (3.22)),

$$k_0\Omega_0^{-1}\hat{\varpi}_m^{(v)}(\tau) = -\left(\mathcal{N}\hat{c}_4^{(v)} + \mathrm{i}\mathcal{B}\hat{\vartheta}^{(v)}\right) = k_0\Omega_0^{-1}\hat{\varpi}_m \exp\left(-\frac{\nu}{\Omega_0}\int_0^\tau k^2(s)\mathrm{d}s\right) = 0. \tag{5.7}$$

Accordingly, for a diffusive fluid such that $\nu = \eta = \kappa$, the growth rate of the destabilizing resonance (if it exists) takes the form (see (4.1) and (4.4))

$$\sigma^{(v)} = \sigma - \frac{\nu}{2\pi\Omega_0}\int_0^{2\pi} k^2(s)\mathrm{d}s = \sigma - Re^{-1}L_0^2\left(k_0^2 + k_p^2\right)\left(1 + 2\varepsilon^2\left(1 - \mu^2\right)\right), \tag{5.8}$$

where $Re = \Omega_0 L_0^2/\nu$ is the Reynolds number and L_0 a characteristic length scale. For the case of MBF (see (2.19) and Appendix A), we obtain

$$\sigma^{(v)} = \sigma - Re^{-1}L_0^2\left(k_0^2 + k_p^2\right)\left(1 + 4\varepsilon^2\mu^2\right). \tag{5.9}$$

Thus, at order $O(\varepsilon)$, the effect of viscosity is the same for both basic flows. At $L_0\sqrt{k_0^2 + k_p^2} \sim 1$, the dominant subharmonic instability survives the diffusive effects if $Re > Re_c = \sigma_m^{-1}$.

6. Concluding remarks

We have analysed here the joint influence of a stable stratification and an external uniform magnetic field on the stability of an unbounded flow with sheared circular streamlines of a perfectly conducting Boussinesq fluid. Two simple background flows permitting a study of parametric instabilities resulting from the excitation of MIG waves by the shear generic to precessing flows were adopted. The first basic state, which is described by (2.18), extends that of Kerswell (1993) and Mason & Kerswell (2002), and represents an

https://doi.org/10.1017/jfm.2025.10881 Published online by Cambridge University Press

idealization of a small-scale disturbance evolving at the centre of a precessing spheroid. The second basic state (see (2.19)) extends that of Mahalov (1993) that represents an infinite column in which a tilted (sheared) streamline solution can exist under precession. These simple models allows us to formulate the stability problem as a system of equations for disturbances in terms of Lagrangian Fourier modes which is universal for wavelengths of the perturbation sufficiently small with respect to the scale of variation of the mean velocity gradients.

Without precession ($\varepsilon = 0$, i.e. the case with circular streamlines), both the basic magnetic field (of intensity B_0) and stable stratification (of strength N), via the mean buoyancy gradient, are in the axial direction which aligns with the solid body rotation with rate Ω_0. In this case and in the non-diffusive linear limit, there are MIG waves with fast and slow waves of dispersion relation given by (3.31). The domains in the plane $(\mathcal{B}, \mathcal{N})$ which characterize the resonant cases of order $n = 1$ of these waves have been identified. (see figure 2), recalling that $\mathcal{B} = B_0 K_0/\Omega_0$ and $\mathcal{N} = N/\Omega_0$ where $K_0 = \sqrt{k_p^2 + k_0^2}$, and k_0 and k_p are defined by (3.12) for KBF and by (A3) for MBF. Some of these resonant cases become destabilizing when excited by the background shear (of rate $2\varepsilon\Omega_0$) generic to precessing flows.

For infinite wavelength in the direction that aligns with the unperturbed magnetic field, so that $k_0 = 0$, the precessing flow is 2D3C. In this case, the stability problem is governed by a Hill equation (i.e. (3.17) for KBF or (A9) for MBF). Stability analysis of the Hill equation indicates that there is a parametric instability of order $O(\varepsilon^2)$ at and near $\mathcal{N} = 1$ with a maximum growth rate of approximately $\sigma_m = \varepsilon^2/2$.

For $k_0 \neq 0$, thanks to MIPS, which is invariant for a non-diffusive system, it was possible to reduce the five-dimensional Floquet system to a four-dimensional inhomogeneous Floquet system with parameters ε, $\mu = k_0/K_0$, $B_0 K_0/\Omega_0$ and N/Ω_0. At order $O(\varepsilon)$, the resulting Floquet system is the same for KBF and MBF. It has been analysed by extending the analytical technique developed by Lebovitz & Zweibel (2004); which allowed us to determine the maximal growth rate of the destabilizing resonances (of order $n = 1$) between two fast modes (σ_{mf}) between two slow modes (σ_{ms}) or between a fast mode and a slow mode (σ_{mm}).

Without stratification ($\mathcal{N} = 0$), the maximum growth rate of the destabilizing resonance between two fast modes, which takes the value $\sigma_{mf} = (5\sqrt{15}/32)\varepsilon$ at $\mathcal{B} = 0$, decreases as $\mathcal{B}$ increases approaching $\sigma_{mf} = \varepsilon/2$ as $\mathcal{B} \to +\infty$. In the presence of stable stratification, this parametric instability is weakened when $(\mathcal{B}, \mathcal{N})$ belongs to the domain $([0, +\infty[\times[0, 0.5[) \cup \mathcal{D}_f$ where $\mathcal{D}_f$ is defined by (4.19), and it does not exist for $(\mathcal{B}, \mathcal{N})$ outside this domain. In addition, σ_{mf} approaches zero as $\mathcal{B} \to +\infty$ (see (4.22)), recalling that the large $\mathcal{B}$ corresponds either to a large unperturbed magnetic field, or to a large K_0 (i.e. small scales).

As for the instability associated with the resonant case (or order $n = 1$) between two slow modes, in the absence of stratification, it exists only for $\mathcal{B} \geqslant \sqrt{5}/2$ and its maximal growth rate increases as $\mathcal{B}$ increases approaching $\sigma_{ms} = \varepsilon/2$ as $\mathcal{B} \to +\infty$. This instability is also weakened by stable stratification, so that as σ_{ms} tends to zero as $\mathcal{B} \to +\infty$. We note that the case of an elliptical flow, stable stratification enhanced the instability associated with the resonant case ($n = 2$) between two slow modes, so as σ_{ms} approaches $\varepsilon/2$ as $\mathcal{B} \to +\infty$.

For the stratified magnetized precessing flow, it is rather the destabilizing resonance between a fast mode and a slow mode which is enhanced by stratification provided $\mathcal{N} < 1$, $\sigma_{mm} = (\varepsilon/2)\sqrt{(1 - \mathcal{N}^2)/(1 + \mathcal{N}^2)}$ as $\mathcal{B} \to +\infty$. In fact, in the case without stratification, it found that σ_{mm} approaches zero as $\mathcal{B} \to +\infty$.

https://doi.org/10.1017/jfm.2025.10881 Published online by Cambridge University Press

Our analytical results clearly prove that, for destabilizing resonances (of order $n = 1$) between two fast modes, between two slow modes or between a fast mode and a slow mode, the limit $\mathcal{N} \to 0$ is in fact singular (discontinuous).

The asymptotic formulae, which characterize only the resonant cases of order $n = 1$ and not those of order $n \geqslant 2$, are in good agreement with the numerical results at least for sufficiently small ε. For KBF, the destabilizing resonances of order $n = 1$ are the strongest, so that there is a good agreement between the asymptotic formulae and the numerical results even if $\varepsilon (\leqslant 0.2)$ is not small. In return, for MBF, the destabilizing resonances of order $n \geqslant 2$ can be the strongest when ε is not sufficiently small, notably for $\mathcal{N} > 1$ and $\mathcal{B}$ large (see figures 7*b* and 8*b*).

The simple case considering diffusive effects where $\nu = \eta = \kappa$, i.e. the magnetic and thermal Prandtl numbers are both equal to one, was briefly discussed. It follows that the instability survives viscous effects as long as the Reynolds number remains greater than the inverse of the maximum growth rate obtained in the inviscid case.

We note that the study of nonlinear effects on the magneto-gravitational-precessional instability in the case of (statistically) homogeneous turbulence constitutes the motivation for further studies for which the present analytical developments can serve as a parametric study.

Supplementary material. Supplementary material is available at https://doi.org/10.1017/jfm.2025.10881.

Declaration of interests. The authors report no conflict of interest.

Appendix A. The case of MBF

In Appendix A we consider the MBF, which is described by (2.19), and derive the resulting Floquet system governing the stability problem in this basic flow case.

A.1. *Floquet system in wave space*

A.1.1. *Time-dependent wavevector*

For the MBF (described by (2.19)), (3.5),

$$d_t k_1 = -\Omega_0 k_2, \quad d_t k_2 = \Omega_0 (k_1 + 2\varepsilon k_3), \quad d_t k_3 = 0, \tag{A1}$$

can be solved to give

$$k_1 = k_p \cos\tau - 2\varepsilon k_3, \quad k_2 = k_p \sin\tau, \quad k_3 = k_{30}, \tag{A2}$$

where

$$k_p = \sqrt{(k_{10} + 2\varepsilon k_{30})^2 + k_{20}^2} = \sqrt{(k_1 + 2\varepsilon k_3)^2 + k_2^2}, \quad k_0 \equiv k_3. \tag{A3}$$

Both k_p and k_0 are time-independent, so that $\mu = k_0/\sqrt{k_0^2 + k_p^2}$ (see (3.21). The wavevector trajectories are circles with sheared centres.

A.1.2. *Floquet system*

Substituting the form (2.19) and the plane wave solution (3.3) into the system (3.6), we obtain the following seven-dimensional system:

$$d_t \hat{u}_1 = -\mathrm{i}k_1 \hat{p} + \Omega_0 \hat{u}_2 + \mathrm{i}(k_3 B_0)\hat{b}_1 - \frac{2\varepsilon N}{\sqrt{1+4\varepsilon^2}}\hat{\vartheta}, \tag{A4a}$$

$$d_t \hat{u}_2 = -\mathrm{i}k_2 \hat{p} - \Omega_0 \hat{u}_1 + 2\varepsilon\Omega_0 \hat{u}_3 + \mathrm{i}(k_3 B_0)\hat{b}_2, \tag{A4b}$$

$$d_t \hat{u}_3 = -\mathrm{i}k_3 \hat{p} + \mathrm{i}(k_3 B_0)\hat{b}_3 + \frac{N}{\sqrt{1+4\varepsilon^2}}\hat{\vartheta}, \tag{A4c}$$

https://doi.org/10.1017/jfm.2025.10881 Published online by Cambridge University Press

$$d_t\hat{b}_1 = -\Omega_0\hat{b}_2 + \mathrm{i}(k_3B_0)\hat{u}_1, \tag{A4d}$$

$$d_t\hat{b}_2 = \Omega_0\hat{b}_1 + \mathrm{i}(k_3B_0)\hat{u}_2, \tag{A4e}$$

$$d_t\hat{b}_3 = -2\varepsilon\Omega_0\hat{b}_2 + \mathrm{i}(k_3B_0)\hat{u}_3, \tag{A4f}$$

$$d_t\hat{\vartheta} = N\big(2\varepsilon\hat{u}_1 - \hat{u}_3\big), \tag{A4g}$$

together with the conditions $\boldsymbol{k}\cdot\hat{\boldsymbol{u}} = 0$ and $\boldsymbol{k}\cdot\hat{\boldsymbol{b}} = 0$. The use of these two conditions allows one to deduce the Fourier amplitude of the pressure disturbance,

$$\hat{p} = -\mathrm{i}k^{-2}\left[2\Omega_0\big(k_1\hat{u}_2 - k_2\hat{u}_1\big) + 2\varepsilon\Omega_0\big(k_2\hat{u}_3 + k_3\hat{u}_2\big) + \frac{(k_3 - 2\varepsilon k_1)N}{\sqrt{1+4\varepsilon^2}}\hat{\vartheta}\right]. \tag{A5}$$

A.1.3. *The case where $k_p = 0$*

For $k_p = 0$, so that $k_2 = 0$ and $k_1 + 2\varepsilon k_3 = 0$, the flow is 1D2C since the constraints $\boldsymbol{k}\cdot\hat{\boldsymbol{u}} = 0$ and $\boldsymbol{k}\cdot\hat{\boldsymbol{b}} = 0$ give

$$k_3\big(\hat{u}_3 - 2\varepsilon\hat{u}_1\big) = 0, \quad k_3\big(\hat{b}_3 - 2\varepsilon\hat{b}_1\big) = 0, \tag{A6}$$

respectively. In this case, system (A4) reduces to a four-dimensional system for the velocity and magnetic field horizontal fluctuations which are not affected by the effect of stratification (at least for the linear regime),

$$d_t\begin{pmatrix}\hat{u}_1\\ \hat{u}_2\\ \hat{b}_1\\ \hat{b}_2\end{pmatrix} = \begin{pmatrix}0 & \frac{(1-4\varepsilon^2)}{(1+4\varepsilon^2)}\Omega_0 & \mathrm{i}(k_3B_0) & 0\\ -(1-4\varepsilon^2)\Omega_0 & 0 & 0 & \mathrm{i}(k_3B_0)\\ \mathrm{i}(k_3B_0) & 0 & 0 & -\Omega_0\\ 0 & \mathrm{i}(k_3B_0) & \Omega_0 & 0\end{pmatrix}\cdot\begin{pmatrix}\hat{u}_1\\ \hat{u}_2\\ \hat{b}_1\\ \hat{b}_2\end{pmatrix} \tag{A7}$$

with $\hat{\vartheta} = \text{const}$. It is not difficult to show that there can be no instability associated with the solution of the above differential system.

A.1.4. *The case where $k_3 = 0$*

For $k_3 = 0$, which corresponds to an infinite wavelength along the solid body rotation axis, the frequency of Alfvén waves vanishes ($\omega_a = k_3B_0 = 0$), and hence, in the linear regime, the flow dynamics is not affected by the Lorentz force. In this case, one easily verifies that

$$\hat{\omega}_3 - 2\varepsilon\hat{\omega}_1 = \mathrm{i}\big(k_1\hat{u}_2 - k_2\hat{u}_1\big) - 2\mathrm{i}\varepsilon k_2\hat{u}_3 = \text{const.}, \tag{A8}$$

is a constant of motion. Accordingly, the resulting stability problem for $k_3 = 0$ is governed by the following Hill equation:

$$d_{\tau\tau}\hat{u}_3 + \frac{\mathcal{N}^2}{\sqrt{1+4\varepsilon^2}}\big(1 + 2\varepsilon^2\big(1 - \sin 2\tau\big)\big)\hat{u}_3 = 0. \tag{A9}$$

The analysis of the solution of this last equation can be done in a similar way to that of the solution of the (3.17). Therefore, at order $O(\varepsilon^2)$, the solution is unstable at and near $\mathcal{N} = 1$ with a maximal growth rate, $\sigma_m = (1/2)\varepsilon^2$.

A.2. *Reduced Floquet system*

A.2.1. *Change of variables*

For $k_3 \neq 0$, we introduce the following variables to facilitate subsequent calculations (see, Salhi *et al.* 2010):

https://doi.org/10.1017/jfm.2025.10881 Published online by Cambridge University Press

$$\Omega_0\hat{c}_1 = (k_1 + 2\varepsilon k_3)\hat{u}_2 - k_2\hat{u}_1, \quad \Omega_0\hat{c}_2 = k_3\big(2\varepsilon\hat{u}_1 - \hat{u}_3\big), \tag{A10a}$$

$$\Omega_0\hat{c}_3 = (k_1 + 2\varepsilon k_3)\hat{b}_2 - k_2\hat{b}_1, \quad \Omega_0\hat{c}_4 = k_3\big(2\varepsilon\hat{b}_1 - \hat{b}_3\big). \tag{A10b}$$

In terms of these variables, the linear part of the spectral counterpart of MIPS (see (3.2)) reads

$$\frac{\hat{\varpi}_m}{\Omega_0} = \frac{\mathcal{N}}{\sqrt{1+4\varepsilon^2}}\big(-2\varepsilon\hat{b}_1 + \hat{b}_3\big) + \mathrm{i}\mathcal{B}\hat{\vartheta} = -\frac{\mathcal{N}}{k_3\sqrt{1+4\varepsilon^2}}\hat{c}_4 + \mathrm{i}\mathcal{B}\hat{\vartheta}, \tag{A11}$$

recalling that the parameters $\mathcal{B}$ and $\mathcal{N}$ are defined by (3.21). For purposes of studying stability, we may set $\hat{\varpi}_m = 0$, as indicated previously.

A.2.2. *Reduced homogeneous Floquet system*

Accordingly, the resulting four-dimensional homogeneous Floquet system for $\hat{\boldsymbol{c}} = (\hat{c}_1, \hat{c}_2, \hat{c}_3, \hat{c}_4)^T$ takes the form

$$d_\tau\hat{\boldsymbol{c}} = \boldsymbol{D}\cdot\hat{\boldsymbol{c}} \tag{A12}$$

where the non-zero elements of the periodic matrix $\boldsymbol{D}$ are

$$D_{11} = -4\varepsilon\frac{k_2k_3}{k^2} - 4\varepsilon^2\frac{k_1k_2k_\perp^2}{k^2k_p^2} - 8\varepsilon^3\frac{k_2k_3k_1^2}{k^2k_p^2}, \tag{A13a}$$

$$D_{12} = -2 - 2\varepsilon\frac{k_1}{k_3} + 8\varepsilon^3\frac{k_1k_3k_2^2}{k^2k_p^2}, \tag{A13b}$$

$$D_{13} = D_{31} = D_{42} = \mathrm{i}\mathcal{B}, \tag{A13c}$$

$$D_{14} = -\frac{2\mathrm{i}\varepsilon\mathcal{N}}{\big(1+4\varepsilon^2\big)\mathcal{B}}\frac{k_2}{k_3}\frac{\big(k_\perp^2 + 2\varepsilon k_1k_3\big)}{k^2}, \tag{A13d}$$

$$D_{21} = 2\frac{k_3^2}{k^2} - 2\varepsilon\frac{k_1k_3}{k^2} + 8\varepsilon^3\frac{k_1k_3k_2^2}{k^2k_p^2}, \tag{A13e}$$

$$D_{22} = 4\varepsilon^2\frac{k_1k_2k_\perp^2}{k^2k_p^2} + 8\varepsilon^3\frac{k_2k_3k_1^2}{k^2k_p^2}, \tag{A13f}$$

$$D_{24} = \mathrm{i}\mathcal{B} + \frac{\mathrm{i}\mathcal{N}}{\big(1+4\varepsilon^2\big)\mathcal{B}}\frac{\big(k_\perp^2 + 4\varepsilon k_1k_3 + 4\varepsilon^2\big(k_2^2+k_3^2\big)\big)}{k^2}, \tag{A13g}$$

where $k_\perp = \sqrt{k_1^2 + k_2^2}$.

Appendix B. Eigenvectors of the matrix $\boldsymbol{D}_0$ and the expression of $\boldsymbol{D}_\varepsilon$

In this appendix we report the eigenvectors of the matrix $\boldsymbol{D}_0$ (see (3.27)) that are associated with the eigenvalues σ_1, $\sigma_2 = -\sigma_1$, σ_3 and $\sigma_4 = -\sigma_3$ given by (3.31). Likewise, we report in this appendix the expression of the derivative of the matrix $\boldsymbol{D}$ with respect to the parameter ε to order $\mathcal{O}(\varepsilon)$, say $\boldsymbol{D}_\varepsilon$.

B.1. *Eigenvectors associated with the eigenvalues of the matrix* $\boldsymbol{D}_0$

The eigenvectors are the columns of the following matrix:

https://doi.org/10.1017/jfm.2025.10881 Published online by Cambridge University Press

$$\boldsymbol{T}=\begin{pmatrix} \sigma_1 & -\sigma_1 & \sigma_3 & -\sigma_3 \\ -\frac{1}{2}\left(\sigma_1^2+m^2\right) & -\frac{1}{2}\left(\sigma_1^2+m^2\right) & -\frac{1}{2}\left(\sigma_3^2+m^2\right) & -\frac{1}{2}\left(\sigma_3^2+m^2\right) \\ \mathrm{i}m & \mathrm{i}m & \mathrm{i}m & \mathrm{i}m \\ -\frac{\mathrm{i}}{2}\frac{m}{\sigma_1}\left(\sigma_1^2+m^2\right) & \frac{\mathrm{i}}{2}\frac{m}{\sigma_1}\left(\sigma_1^2+m^2\right) & -\frac{\mathrm{i}}{2}\frac{m}{\sigma_3}\left(\sigma_3^2+m^2\right) & \frac{\mathrm{i}}{2}\frac{m}{\sigma_3}\left(\sigma_3^2+m^2\right) \end{pmatrix} \tag{B1}$$

with $m=\mathcal{B}\mu$. The matrix $\boldsymbol{T}$ is inversible,

$$\boldsymbol{T}^{-1}=\frac{1}{\left(\sigma_1^2-\sigma_3^2\right)}\begin{pmatrix} \frac{1}{2}\frac{\sigma_1}{m^2}\left(\sigma_3^2+m^2\right) & -1 & \frac{\mathrm{i}}{2m}\left(\sigma_3^2+m^2\right) & -\frac{\mathrm{i}\sigma_1\sigma_3^2}{m^3} \\ -\frac{1}{2}\frac{\sigma_1}{m^2}\left(\sigma_3^2+m^2\right) & -1 & \frac{\mathrm{i}}{2m}\left(\sigma_3^2+m^2\right) & \frac{\mathrm{i}\sigma_1\sigma_3^2}{m^3} \\ -\frac{1}{2}\frac{\sigma_3}{m^2}\left(\sigma_1^2+m^2\right) & 1 & -\frac{\mathrm{i}}{2m}\left(\sigma_1^2+m^2\right) & \frac{\mathrm{i}\sigma_3\sigma_1^2}{m^3} \\ \frac{1}{2}\frac{\sigma_3}{m^2}\left(\sigma_1^2+m^2\right) & 1 & -\frac{\mathrm{i}}{2m}\left(\sigma_1^2+m^2\right) & -\frac{\mathrm{i}\sigma_3\sigma_1^2}{m^3} \end{pmatrix}, \tag{B2}$$

so that,

$$\tilde{\boldsymbol{D}}_0=\boldsymbol{T}^{-1}\cdot\boldsymbol{D}_0\cdot\boldsymbol{T}=\mathrm{diag}\,(\sigma_1,-\sigma_1,\sigma_3,-\sigma_3), \tag{B3}$$

in the base diagonalizing $\boldsymbol{D}_0$. Such a basis is used to facilitate the calculations leading to the expression of the amplification rates of destabilizing resonances of order $n=1$.

B.2. *Expression of the matrix* $\boldsymbol{D}_\varepsilon$

From (3.24) and (A13) giving the non-zero elements of the matrix $\boldsymbol{D}$ for the KBF and MBF cases, respectively, we deduce that the matrix $\boldsymbol{D}_\varepsilon$ (appearing in the expansion (4.9)) is the same for these two basic flows. The non-zero elements of $\boldsymbol{D}_\varepsilon$ are

$$(\boldsymbol{D}_\varepsilon)_{11}=2\mathrm{i}\mu\sqrt{1-\mu^2}\left(\mathrm{e}^{i\tau}-\mathrm{e}^{-i\tau}\right), \tag{B4a}$$

$$(\boldsymbol{D}_\varepsilon)_{12}=-\frac{\sqrt{1-\mu^2}}{\mu}\left(\mathrm{e}^{i\tau}+\mathrm{e}^{-i\tau}\right), \tag{B4b}$$

$$(\boldsymbol{D}_\varepsilon)_{14}=-\frac{\mathcal{N}^2}{\mathcal{B}}\frac{\left(1-\mu^2\right)\sqrt{1-\mu^2}}{\mu^2}\left(\mathrm{e}^{i\tau}-\mathrm{e}^{-i\tau}\right), \tag{B4c}$$

$$(\boldsymbol{D}_\varepsilon)_{21}=\mu\sqrt{1-\mu^2}\left(4\mu^2-1\right)\left(\mathrm{e}^{i\tau}+\mathrm{e}^{-i\tau}\right), \tag{B4d}$$

$$(\boldsymbol{D}_\varepsilon)_{24}=-2\mathrm{i}\frac{\mathcal{N}^2}{\mathcal{B}}\frac{\left(1-\mu^2\right)\sqrt{1-\mu^2}}{\mu^2}\left(\mathrm{e}^{i\tau}+\mathrm{e}^{-i\tau}\right). \tag{B4e}$$

Thus, the asymptotic analysis to order $\mathcal{O}(\varepsilon)$ is the same for both basic flows (KBF and MBF).

References

Barker, A.J. 2016*a* On turbulence driven by axial precession and tidal evolution of the spin–orbit angle of close-in giant planets. *Mon. Not. R. Astron. Soc.* **460** (3), 2339–2350.

Barker, A.J. 2016*b* Non-linear tides in a homogeneous rotating planet or star: global simulations of the elliptical instability. *Mon. Not. R. Astron. Soc.* **459** (1), 939–956.

Bayly, B.J. 1986 Three-dimensional instability of elliptical flow. *Phys. Rev. Lett.* **57** (17), 2160.

https://doi.org/10.1017/jfm.2025.10881 Published online by Cambridge University Press

BENKACEM, N., SALHI, A., KHLIFI, A., NASRAOUI, S. & CAMBON, C. 2022 Destabilizing resonances of precessing inertia-gravity waves. *Phys. Rev. E* **105** (3), 035107.
BRAGINSKY, S.I. 1991 Towards a realistic theory of the geodynamo. *Geophys. Astrophys. Fluid Dyn.* **60** (1–4), 89–134.
BUFFETT, B., KNEZEK, N. & HOLME, R. 2016 Evidence for MAC waves at the top of Earths core and implications for variations in length of day. *Geophys. J. Intl* **204** (3), 1789–1800.
BUFFETT, B.A. 2021 Conditions for turbulent Ekman layers in precessionally driven flow. *Geophys. J. Intl* **226** (1), 56–65.
BURMANN, F. & NOIR, J. 2022 Experimental study of the flows in a non-axisymmetric ellipsoid under precession. *J. Fluid Mech.* **932**, A24.
BUSSE, F.H. 1968 Steady fluid flow in a precessing spheroidal shell. *J. Fluid Mech.* **33** (4), 739–751.
CAMBON, C., TEISSEDRE, C. & JEANDEL, D. 1985 Etude d'effets couplés de déformation et de rotation sur une turbulence homogène. *Journal de mécanique théorique et appliquée* **4** (5), 629–657.
CATON, F., JANIAUD, B. & HOPFINGER, E.J. 2000 Stability and bifurcations in stratified Taylor–Couette flow. *J. Fluid Mech.* **419**, 93–124.
CÉBRON, D., LAGUERRE, R., NOIR, J. & SCHAEFFER, N. 2019 Precessing spherical shells: flows, dissipation, dynamo and the lunar core. *Geophys. J. Intl* **219** (Supplement 1), S34–S57.
CRAIK, A.D.D. & CRIMINALE, W.O. 1986 Evolution of wavelike disturbances in shear flows: a class of exact solutions of the Navier–Stokes equations. *Proc. R. Soc. Lond. A. Math. Phys. Sci.* **406** (1830), 13–26.
CRAIK, A.D.D. 1989 The stability of unbounded two-and three-dimensional flows subject to body forces: some exact solutions. *J. Fluid Mech.* **198**, 275–292.
DAVIDSON, P.A. 2013 *Turbulence in Rotating, Stratified and Electrically Conducting Fluids*. Cambridge University Press.
DAVIES, P.A. 1972 Experiments on Taylor columns in rotating stratified fluids. *J. Fluid Mech.* **54** (4), 691–717.
DRAZIN, P.G. & REID, W.H. 2004 *Hydrodynamic Stability*. Cambridge University Press.
ETCHEVEST, M., FONTANA, M. & DMITRUK, P. 2022 Behavior of hydrodynamic and magnetohydrodynamic turbulence in a rotating sphere with precession and dynamo action. *Phys. Rev. Fluids* **7** (10), 103801.
FEARN, D.R. & PROCTOR, M.R.E. 1983 Hydromagnetic waves in a differentially rotating sphere. *J. Fluid Mech.* **128**, 1–20.
FINLAY, C.C., MAUS, S., BEGGAN, C.D., BONDAR, T.N., CHAMBODUT, A., CHERNOVA, T.A. & ZVEREVA, T.I. 2010 International geomagnetic reference field: the eleventh generation. *Geophys. J. Intl* **183** (3), 1216–1230.
GANS, R.F. 1970 On the precession of a resonant cylinder. *J. Fluid Mech.* **41** (4), 865–872.
GAO, D., MEUNIER, P., LE DIZÈS, S. & ELOY, C. 2021 Zonal flow in a resonant precessing cylinder. *J. Fluid Mech.* **923**, A29.
GIESECKE, A., VOGT, T., GUNDRUM, T. & STEFANI, F. 2019 Kinematic dynamo action of a precession-driven flow based on the results of water experiments and hydrodynamic simulations. *Geophys. Astrophys. Fluid Dyn.* **113** (1–2), 235–255.
GIESECKE, A., VOGT, T., PIZZI, F., KUMAR, V., GONZALEZ, F.G., GUNDRUM, T. & STEFANI, F. 2024 The global flow state in a precessing cylinder. *J. Fluid Mech.* **998**, A30.
GLAMPEDAKIS, K., ANDERSSON, N. & JONES, D.I. 2008 Stability of precessing superfluid neutron stars. *Phys. Rev. Lett.* **100** (8), 081101.
GREENSPAN, H.P. 1969 *The Theory of Rotating Fluids*. Cambridge University Press.
HOLLERBACH, R. & CALLY, P.S. 2009 Nonlinear evolution of axisymmetric twisted flux tubes in the solar tachocline. *Solar Phys.* **260**, 251–260.
KERSWELL, R.R. 1993 The instability of precessing flow. *Geophys. Astrophys. Fluid Dyn.* **72** (1-4), 107–144.
KERSWELL, R.R. 2002 Elliptical instability. *Annu. Rev. Fluid Mech.* **34** (1), 83–113.
KHLIFI, A., SALHI, A., NASRAOUI, S., GODEFERD, F. & CAMBON, C. 2018 Spectral energy scaling in precessing turbulence. *Phys. Rev. E* **98** (1), 011102.
KUCHMENT, P.A. 1993 *Floquet Theory for Partial Differential Equations*, vol. 60. Springer.
KUMAR, V., PIZZI, F., MAMATSASHVILI, G., GIESECKE, A., STEFANI, F. & BARKER, A.J. 2024 Dynamo action driven by precessional turbulence. *Phys. Rev. E* **109** (6), 065101.
LAM, K., KONG, D. & ZHANG, K. 2021 Localised thermal convection in rotating spheres that undergo weak precession. *Geophys. Astrophys. Fluid Dyn.* **115** (3), 280–296.
LEBOVITZ, N.R. & ZWEIBEL, E. 2004 Magnetoelliptic instabilities. *Astrophys. J.* **609** (1), 301.
LEHNER, T., MOUHALI, W., LÉORAT, J. & MAHALOV, A. 2010 Mode coupling analysis and differential rotation in a flow driven by a precessing cylindrical container. *Geophys. Astrophys. Fluid Dyn.* **104** (4), 369–401.
LIFSCHITZ, A. & HAMEIRI, E. 1991 Local stability conditions in fluid dynamics. *Phys. Fluids A: Fluid Dyn.* **3** (11), 2644–2651.

https://doi.org/10.1017/jfm.2025.10881 Published online by Cambridge University Press

LIN, Y., NOIR, J. & JACKSON, A. 2014 Experimental study of fluid flows in a precessing cylindrical annulus. *Phys. Fluids* **26**, 046604.
LORENZANI, S. & TILGNER, A. 2001 Fluid instabilities in precessing spheroidal cavities. *J. Fluid Mech.* **447**, 111–128.
MAHALOV, A. 1993 The instability of rotating fluid columns subjected to a weak external Coriolis force. *Phys. Fluids A: Fluid Dyn.* **5** (4), 891–900.
MALKUS, W.V.R. 1968 Precession of the Earth as the cause of geomagnetism: experiments lend support to the proposal that precessional torques drive the earth's dynamo. *Science* **160** (3825), 259–264.
MASON, R.M. & KERSWELL, R.R. 2002 Chaotic dynamics in a strained rotating flow: a precessing plane fluid layer. *J. Fluid Mech.* **471**, 71–106.
MCKEOWN, R., OSTILLA-MÓNICO, R., PUMIR, A., BRENNER, M.P. & RUBINSTEIN, S.M. 2020 Turbulence generation through an iterative cascade of the elliptical instability. *Sci. Adv.* **6** (9), eaaz2717.
MIYAZAKI, T. & FUKUMOTO, Y. 1992 Three-dimensional instability of strained vortices in a stably stratified fluid. *Phys. Fluids A: Fluid Dyn.* **4** (11), 2515–2522.
MIZERSKI, K.A., BAJER, K. & MOFFATT, H.K. 2012 The mean electromotive force generated by elliptic instability. *J. Fluid Mech.* **707**, 111–128.
MOFFATT, H.K. 1978 Magnetic field generation in electrically conducting fluids. In *Cambridge Monographs on Mechanics and Applied Mathematics*.
MOFFATT, K. & DORMY, E. 2019 *Self-Exciting Fluid Dynamos*, vol. 59. Cambridge University Press.
MOUHALI, W., LEHNER, T., LÉORAT, J. & VITRY, R. 2012 Evidence for a cyclonic regime in a precessing cylindrical container. *Exp. Fluids* **53**, 1693–1700.
MOUHALI, W., SALHI, A., LEHNER, T. & CAMBON, C. 2024 Waves and non-propagating mode in stratified and rotating magnetohydrodynamic turbulence. *Phys. Fluids* **36**, 125194.
NORNBERG, M.D., JI, H., SCHARTMAN, E., ROACH, A. & GOODMAN, J. 2010 Observation of magnetocoriolis waves in a liquid metal Taylor–Couette experiment. *Phys. Rev. Lett.* **104** (7), 074501.
PEDLOSKY, J. 2013 *Geophysical Fluid Dynamics*. Springer Science & Business Media.
PIERREHUMBERT, R.T. 1986 Universal short-wave instability of two-dimensional eddies in an inviscid fluid. *Phys. Rev. Lett.* **57** (17), 2157.
PIZZI, F., MAMATSASHVILI, G., BARKER, A.J., GIESECKE, A. & STEFANI, F. 2022 Interplay between geostrophic vortices and inertial waves in precession-driven turbulence. *Phys. Fluids* **34**, 125135.
POINCARÉ, H. 1910 Sur la précession des corps déformables. *Bulletin astronomique, Observatoire de Paris* **27** (1), 321–356.
SALHI, A. & CAMBON, C. 2009 Precessing rotating flows with additional shear: stability analysis. *Phys. Rev. E* **79** (3), 036303.
SALHI, A., LEHNER, T. & CAMBON, C. 2010 Magnetohydrodynamic instabilities in rotating and precessing sheared flows: an asymptotic analysis. *Phys. Rev. E* **82** (1), 016315.
SALHI, A., LEHNER, T., GODEFERD, F. & CAMBON, C. 2012 Magnetized stratified rotating shear waves. *Phys. Rev. E* **85** (2), 026301.
SALHI, A., LEHNER, T., GODEFERD, F. & CAMBON, C. 2013 Wave–vortex mode coupling in astrophysical accretion disks under combined radial and vertical stratification. *Astrophys. J.* **771** (2), 103.
SALHI, A., BAKLOUTI, F.S., GODEFERD, F., LEHNER, T. & CAMBON, C. 2017 Energy partition, scale by scale, in magnetic Archimedes Coriolis weak wave turbulence. *Phys. Rev. E* **95** (2), 023112.
SALHI, A., KHLIFI, A. & CAMBON, C. 2019 Nonlinear effects on the precessional instability in magnetized turbulence. *Atmosphere-BASEL* **11** (1), 14.
SALHI, A. & CAMBON, C. 2023 Magneto-gravity-elliptic instability. *J. Fluid Mech.* **963**, A9.
SALHI, A., KHLIFI, A., MARINO, R., FERACO, F., FOLDES, R. & CAMBON, C. 2024 Waves and non-propagating modes in stratified MHD turbulence subject to a weak mean magnetic field. *J. Fluid Mech.* **1001**, A28.
SLANE, J. & TRAGESSER, S. 2011 Analysis of periodic nonautonomous inhomogeneous systems. *Nonlinear Dyn. Syst. Theory* **11** (2), 183–198.
SPIEGEL, E.A. & VERONIS, G. 1960 On the Boussinesq approximation for a compressible fluid. *Astrophys. J.* **131**, 442.
TILGNER, A. 1999 Magnetohydrodynamic flow in precessing spherical shells. *J. Fluid Mech.* **379**, 303–318.
TOMCZYK, S., MCINTOSH, S.W., KEIL, S.L., JUDGE, P.G., SCHAD, T., SEELEY, D.H. & EDMONDSON, J. 2007 Alfvén waves in the solar corona. *Science* **317** (5842), 1192–1196.
VLADIMIROV, V.A. & TARASSOV, V.F. 1984 Forced regimes of motion of a rotating fluid. *Sov. Phys. D* **30**, 654.
VORMANN, J. & HANSEN, U. 2020 Characteristics of a precessing flow under the influence of a convecting temperature field in a spheroidal shell. *J. Fluid Mech.* **891**, A15.

https://doi.org/10.1017/jfm.2025.10881 Published online by Cambridge University Press

WALEFFE, F. 1992 The nature of triad interactions in homogeneous turbulence. *Phys. Fluids A: Fluid Dyn.* **4** (2), 350–363.

WEI, X. & TILGNER, A. 2013 Stratified precessional flow in spherical geometry. *J. Fluid Mech.* **718**, R2.

WEI, X. 2016 The combined effect of precession and convection on the dynamo action. *Astrophys. J.* **827** (2), 123.

WIENER, R.J., HAMMER, P.W., SWANSON, C.E. & DONNELLY, R.J. 1990 Stability of Taylor–Couette flow subject to an external Coriolis force. *Phys. Rev. Lett.* **64** (10), 1115.

ZHANG, K., CHAN, K.H. & LIAO, X. 2014 On precessing flow in an oblate spheroid of arbitrary eccentricity. *J. Fluid Mech.* **743**, 358–384.

https://doi.org/10.1017/jfm.2025.10881 Published online by Cambridge University Press